

# JGR Solid Earth

## RESEARCH ARTICLE

10.1029/2024JB028844

### Key Points:

- The results of a P-wave teleseismic tomography study of the central to southern Andean subduction zones are presented
- A fast-velocity anomaly beneath the Nazca slab was revealed and interpreted as a relic Nazca slab segment
- A slow-velocity anomaly associated with the slab window was observed, constraining the maximum depth the asthenospheric window affects

### Supporting Information:

Supporting Information may be found in the online version of this article.

### Correspondence to:

Y. Kondo,  
ykondo@stu.kobe-u.ac.jp

### Citation:

Kondo, Y., Obayashi, M., Sugioka, H., Shiobara, H., Ito, A., Shinohara, M., et al. (2024). Seismic image of the central to southern Andean subduction zone through finite-frequency tomography. *Journal of Geophysical Research: Solid Earth*, 129, e2024JB028844. <https://doi.org/10.1029/2024JB028844>

Received 30 JAN 2024

Accepted 23 OCT 2024

### Author Contributions:

**Conceptualization:** Y. Kondo  
**Data curation:** Y. Kondo, H. Sugioka, H. Shiobara, A. Ito, M. Shinohara, H. Iwamori, M. Kinoshita, M. Miller, C. Tassara, J. Ojeda  
**Formal analysis:** Y. Kondo  
**Funding acquisition:** Y. Kondo, H. Sugioka, M. Kinoshita  
**Investigation:** Y. Kondo  
**Methodology:** Y. Kondo, M. Obayashi  
**Software:** M. Obayashi  
**Supervision:** M. Obayashi, H. Sugioka  
**Validation:** Y. Kondo, M. Obayashi  
**Visualization:** Y. Kondo  
**Writing – original draft:** Y. Kondo  
**Writing – review & editing:** Y. Kondo, M. Obayashi, H. Sugioka, H. Shiobara, H. Iwamori, M. Miller, J. Ojeda

© 2024. American Geophysical Union. All Rights Reserved.

## Seismic Image of the Central to Southern Andean Subduction Zone Through Finite-Frequency Tomography

Y. Kondo<sup>1</sup> , M. Obayashi<sup>1,2</sup> , H. Sugioka<sup>1</sup> , H. Shiobara<sup>3</sup> , A. Ito<sup>2</sup> , M. Shinohara<sup>3</sup> , H. Iwamori<sup>3</sup>, M. Kinoshita<sup>3</sup> , M. Miller<sup>4</sup>, C. Tassara<sup>5</sup> , and J. Ojeda<sup>6,7</sup> 

<sup>1</sup>Kobe University, Kobe, Japan, <sup>2</sup>Japan Agency of Marine-Earth Science and Technology, Yokosuka, Japan, <sup>3</sup>Earthquake Research Institute, The University of Tokyo, Tokyo, Japan, <sup>4</sup>Department of Geophysics, University of Concepción, Concepción, Chile, <sup>5</sup>Faculty of Science, Arturo Prat University, Iquique, Chile, <sup>6</sup>Departamento de Geofísica, Universidad de Chile, Santiago, Chile, <sup>7</sup>Institut de Physique du Globe de Paris, Université Paris Cité, CNRS, Paris, France

**Abstract** This study presents new seismic imaging of the Andean subduction zone through P-wave hybrid finite-frequency and ray-theoretical tomography. We measured both differential and absolute traveltimes using broadband seismic waveforms from stations in an array of ocean-bottom seismographs near the Chile Triple Junction (CTJ) and stations within 30° of the array. These data were combined with the global traveltime data set to obtain a global P-wave velocity structure with a focus on central to southern South America. The new tomographic image showed the Nazca slab geometry as a continuous fast anomaly, which is consistent with seismic activity and prior slab models. Furthermore, two notable structures were observed: a broad extension of the fast anomaly beneath the Nazca slab at 26–35°S and a slow anomaly east of the CTJ. The checkerboard resolution and recovery tests confirmed the reliability of these large-scale features. The fast anomaly, isolated from the Nazca slab, was interpreted as a relic Nazca slab segment based on its strong amplitude and spatial coincidence with the current Pampean and past Payenia flat slab segments. The slow anomaly near the CTJ was consistent with the previously inferred extent of the Patagonian slab window. Moreover, the active adakitic volcanoes are aligned with the southern edge of the anomaly, and the plateau basalts are located within the anomaly. Our model showed that the slow anomaly extended to a depth of up to 250 km, suggesting a depth limit that the asthenospheric window can influence.

**Plain Language Summary** The western margin of South America is one of the largest subduction zones on the Earth and has provided insights into the subduction dynamics of relatively young oceanic plates. We developed a new seismic P-wave velocity model beneath the Central to Southern South America. Using broadband seismograms, we measured differential traveltimes between two stations by cross-correlation method and picked P-wave onsets, and performed tomographic inversion in combination with the global traveltime data from the International Seismological Centre catalog. Our model shows mantle structure to the uppermost part of the lower mantle at a depth of ~1,000 km. The geometry of the Nazca slab in our model agrees well with other seismic imagings and slab models. Beneath the Nazca slab, a fast velocity anomaly was observed and interpreted as a relic Nazca slab segment. Moreover, strong, slow anomalies in the upper mantle were observed to be located on east side of where the actively spreading Chile Ridge is subducting. The extent of the anomalies, and comparison with volcanism, suggest that the influence of the asthenospheric window extends to a depth of up to 250 km.

## 1. Introduction

The Chile Trench is part of a subduction zone more than ~7,000 km in length, where the Antarctic and Nazca plates are currently subducting eastward beneath the South American plate (Figure 1). The subduction system in Chile is characterized by a young, warm oceanic lithosphere that subducts less steeply, including horizontal flat-slab segments (e.g., Barazangi & Isacks, 1976; Cahill & Isacks, 1992; Suárez et al., 1983). The convergence rates along the trench are relatively constant at ~6.7 cm/yr at an azimuth of ~77° (DeMets et al., 2010). The age of the Nazca plate varies systematically along the Chile Trench, from 0 Myr at the Carnegie Ridge (~7°S) to 50 Myr at 20°S and 0 Myr at the Chile Ridge (Müller et al., 2008). At ~46°S, the Chile Ridge subducts against the Chile Trench to form the Chile Triple Junction (CTJ). This region is a unique example of the subduction of an actively spreading ridge.

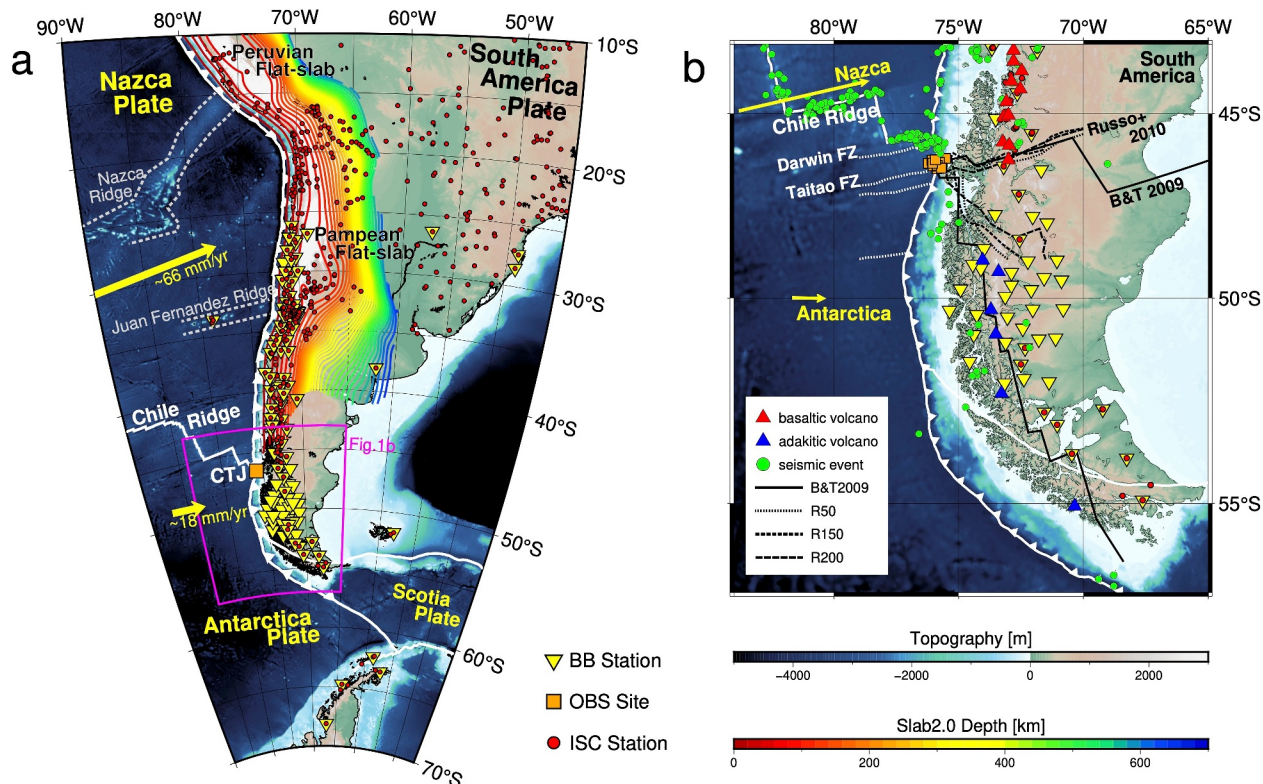


**Figure 1.** Tectonic settings of the central to southern Andean subduction zone. The yellow triangles represent the broadband seismic stations from IRIS, and the orange squares indicate the location of 12 Ocean Bottom Seismometers, which were used to measure traveltimes. Red circles indicate stations in the International Seismology Centre's global traveltimes data. Within the area of the anticipated Patagonian slab window, there are dense broadband stations that have not yet been included in ISC's global data. (a) Map of Central-Southern South America, showing Nazca slab contours of the Slab2 model as colored lines (Hayes et al., 2018), current plate boundaries as solid white lines (United States Geological Survey), and the primary aseismic ridges as dotted white lines. The yellow arrows indicate the motion of the Nazca and Antarctica plates relative to South America (DeMets et al., 2010). (b) Map of Southern Patagonia with the estimated extensions of the Patagonian slab window delineated by the black solid line (BT2009) as proposed by Breitsprecher and Thorkelson (2009). The black dotted lines, R50, R100, and R200, represent the iso-depths of the slab window edge according to the Vp anomaly contour by Russo et al. (2010). The red and blue triangles signify the basaltic and adakitic volcanism along the volcanic arc, respectively (Siebert & Simkin, 2002), while the green dots indicate the epicenters of the seismic event with magnitudes greater than 4, showing a seismic gap within the window.

### 1.1. Subduction of the Nazca Plate

Seismic activity, volcanism, topography, and deformation along the western edge of South America exhibit significant variations along the trench strike. These variations are primarily attributed to complex geological processes associated with spatial and temporal changes in the geometry, dip angle, and hydration state of the subducting Nazca plate (e.g., Chen et al., 2019; Dávila & Lithgow-Bertelloni, 2013; Espurt et al., 2008; Kay & Coira, 2009; Martinod et al., 2013; Ramos, 1999; Ramos & Folguera, 2009). In particular, the flat subduction of the Nazca plate has been considered to have a substantial influence on the overriding plate, causing the cessation of arc volcanism, the uplift and deformation of the Andes, crustal thickening, and basement uplift over a broad area (e.g., Cristallini & Ramos, 2000; Kay & Mpodozis, 2002; Ramos et al., 2002).

Understanding the character and behavior of the Nazca slab in comprehending the complexity and uniqueness of the subduction system of the Andean margin has prompted various seismic imaging studies in this region. Many regional teleseismic tomography studies have provided insights into the structure of the Nazca slab in the upper mantle, revealing features such as slab holes and tearing (Pesicek et al., 2012; Portner et al., 2017; Scire et al., 2016), lithospheric delamination (e.g., Bianchi et al., 2013), and variations in slab thickness (Scire et al., 2017). More recently, continental-scale teleseismic tomography studies covering the lower mantle have improved the resolution and provided key constraints on the detailed structure of the Nazca slab (Ciardelli et al., 2022; Mohammadzaheri et al., 2021; Portner et al., 2020; Rodríguez et al., 2020). The observed behavior of the slab in global models is generally consistent with these regional models (e.g., Lu et al., 2019; Obayashi et al., 2013; Simmons et al., 2012).

Such models show similar trends; for example, transitions from normal to flat subduction along the strike and dip directions, the slab stagnation at  $\sim 1,000\text{--}1,100$  km depth in the lower mantle in the northern region of  $\sim 28^\circ\text{S}$ , and penetration into greater depths north of  $20^\circ\text{S}$ .

Flat subduction segments, which are unique features along the western margin of South America, have been extensively debated (e.g., Espurt et al., 2008; Gutscher et al., 2000; Manea et al., 2017; Marot et al., 2014; Ramos & Folguera, 2009). Three well-known flat slab segments exist: the Mexican ( $5\text{--}8^\circ\text{N}$ ), Peruvian ( $5\text{--}15^\circ\text{S}$ ), and Pampean flat slabs ( $26\text{--}32^\circ\text{S}$ ). They lie horizontally for hundreds of kilometers before steeply subducting into the deep mantle, although their horizontal dimensions and flattening depths are different. The presence of flat-slab subduction has been reported based on seismicity (e.g., Barazangi & Isacks, 1976; Pardo et al., 2002; Pesicek et al., 2012), volcanism (e.g., Kay & Mpodozis, 2002), electrical conductivity analysis (e.g., Burd et al., 2013), and seismic imaging studies (e.g., Gutscher, 2002; Ma & Clayton, 2014; Porter et al., 2012). The seismic velocity structures of flat slabs and their surrounding regions down to  $\sim 150$  km and those in the upper mantle have been resolved by surface wave tomography (e.g., Celli et al., 2020; Feng et al., 2007) and regional body wave tomography (e.g., Gao et al., 2021; Portner et al., 2017; Scire et al., 2016), respectively. The locations of the flat-slab segments coincide spatially with the intersections of the aseismic ridges and Chile Trench. Consequently, it has been widely argued that the current Peruvian and Pampean flat slabs are associated with the subduction of the Nazca and Juan Fernández ridges, which originated from hotspot volcanism (Figure 1a, e.g., Gutscher et al., 2000; Kay & Mpodozis, 2002). Recent numerical modeling studies have revealed that the overriding continental plate thickness, plate kinematics, and/or asthenospheric dynamics may play essential roles in the development of flat-slab and oceanic plateau subduction (Manea et al., 2017, 2012, and references therein). However, the mechanisms and tectonics of flat-slab subduction remain controversial (e.g., Gao et al., 2021; Liu & Currie, 2019).

Slow anomalies just below the Peruvian and Pampean flat slabs have been identified (Celli et al., 2020), and their interactions with these slabs have been discussed (Rodríguez et al., 2020). Several possible models have been proposed to explain these slow anomalies, including asthenospheric upwelling associated with locally thinned oceanic lithosphere related to the Nazca Ridge (Scire et al., 2016), the presence of volatile-rich subslab mantle flow, increased temperature and/or decompression melting due to small-scale vertical flow (Antonijevic et al., 2016), and the entrainment of hotspot material (Portner et al., 2017). Moreover, a high-velocity anomaly, disconnected from the subducting Nazca slab, was reported beneath the slab. Teleseismic shear wave tomography by Rodríguez et al. (2020) and full waveform inversion by Gao et al. (2021) detected a fast S-wave velocity anomaly beneath the Chile Trench in the latitude range of  $25\text{--}35^\circ\text{S}$ . These studies interpreted this anomaly as either a remnant of a completely subducted slab or a detached Nazca slab. However, the geometry and amplitude of non-slab seismic anomalies, including slow and fast subslab anomalies, vary widely among models and remain subjects of debate.

## 1.2. Patagonian Slab Window

The actively spreading Chile Ridge has been subducting since the mid-Miocene (Figure 1b; Breitsprecher & Thorkelson, 2009; Cande et al., 1987; Eagles et al., 2009), forming the CTJ and providing an important opportunity to study ridge subduction. Since the 1980s, numerous geological, geochemical, and geophysical studies have been conducted on the subduction of the Chile Ridge (e.g., Bangs & Cande, 1997; Gallego et al., 2010; Kaeding et al., 1990; Maksymowicz et al., 2012). These studies revealed that the subduction of the Chile Ridge segments has widespread effects on the overriding continental plate: the pronounced gap in the Patagonian volcanic arc and seismicity along the subduction zone (Agurto-Detzel et al., 2014; Cande & Leslie, 1986; DeLong et al., 1979; Gutiérrez et al., 2005; Ramos & Kay, 1992), adakitic volcanism near the slab edges (Bourgois et al., 2016; Stern & Kilian, 1996; Thorkelson & Breitsprecher, 2005), back-arc-like plateau basalts in Patagonia (Espinoza et al., 2005; Gorring et al., 1997; Ramos & Kay, 1992), geologically recent volcanic activity anomalously close to the trench (Forsythe et al., 1986; Lagabrielle et al., 1994, 2000), anomalous isotopic compositions of the lavas from the southern Chile Ridge (Karsten et al., 1996), obduction of the Plio-Pleistocene Taitao ophiolite (Bourgois et al., 1996; Lagabrielle et al., 2000; Nelson et al., 1993; Veloso et al., 2005), an anomalously large negative Bouguer gravity anomaly and extremely high heat flow on the eastern side of the CTJ (Ávila & Dávila, 2018; Cande et al., 1987; Murdie et al., 2000), and positive dynamic topography (Boutonnet et al., 2010; Guillaume et al., 2009, 2010; Mark et al., 2022).

When a spreading ridge intersects a trench, the ridge-transform system is surrounded by a hot asthenospheric mantle as it descends. The ridge-transform system continues to spread, and no new lithosphere is formed along the subducted ridge. Consequently, the slab window, the gap between the edges of the subducted-ridge transform system, progressively expands (DeLong et al., 1979; Dickinson & Snyder, 1979; Groome & Thorkelson, 2009; Thorkelson, 1996; Thorkelson & Breitsprecher, 2005; Thorkelson & Taylor, 1989). Slab windows provide gaps through which the asthenospheric mantle can flow and mix, resulting in local thermal anomalies in the asthenosphere and strong chemical and physical effects on the surrounding mantle (Thorkelson, 1996; Thorkelson & Taylor, 1989).

The formation of the Patagonian slab window commenced at approximately 18 Ma when the Chile Ridge began to subduct at approximately 54°S on the South American continent (Breitsprecher & Thorkelson, 2009). Since then, the window has gradually extended as the triple junction has migrated northward by approximately 1,000 km, with major ridge segments subducting at 14, 10, 6, 3, and 100 ka to the present (Bourgois et al., 2000; Breitsprecher & Thorkelson, 2009). The extent of the Patagonian slab window has been estimated using kinematic reconstruction (Breitsprecher & Thorkelson, 2009) and imaged using seismic tomography as upper mantle low-seismic-velocity anomalies (Gallego et al., 2010; Mark et al., 2022; Miller et al., 2023; Russo et al., 2010).

Russo et al. (2010) first delineated the Patagonian slab window to a depth of 200 km using regional body-wave tomography with teleseismic data recorded on temporary seismic networks. Recently, Miller et al. (2023) enhanced the tomographic image of the Chile Ridge subduction using a technique similar to that Russo et al. (2010) employed with a different data set. Their results showed pronounced slow anomalies with an amplitude of ~3% between depths of 100 and 300 km on the east side of the CTJ, along with a fast anomaly interpreted as a young Nazca plate on its northern side. They discussed in detail the geometry of the subducted Nazca plate near the CTJ and proposed slab tears along the fracture zone among subducted Nazca plate segments. The results obtained from the kinematic reconstruction and seismic models are in good agreement. Previous body wave studies on slab windows focused on an area of hundreds of kilometers around the CTJ. Mark et al. (2022) provided an extensive image using Rayleigh wave tomography across the entire Patagonian slab window. They observed slow S-wave velocities within a slab window at shallow depths and discussed the thermal erosion of the lithosphere in the young slab window. To comprehensively discuss the mantle response to slab window formation, a more extensive and deep seismic velocity structure that provides constraints on the full extent and depth of the window is required. However, other regional and global tomography models, which cover broader areas, have limited resolution in southern South America owing to the paucity of stations and low seismic activity.

In this paper, we report a new three-dimensional P-wave velocity model beneath central to southern South America based on traveltimes data measured using broadband seismograms collected in the target region and our recent seafloor observations near the CTJ. Our findings suggest two remarkable structures: fast anomalies beneath the Nazca slab and slow anomalies east of the CTJ. We then discuss the origin of the subslab fast anomalies and the extent of the Patagonian slab window based on these slow anomalies.

## 2. Data

An Ocean Bottom Seismograph (OBS) array was deployed directly above the CTJ for almost 2 years, from January 2019 to January 2021 (Ito et al., 2023). This OBS array comprised seven broadband OBSs and five long-term OBSs. We collected seismograms from ~100 onshore broadband stations within 30° of the OBS arrays for the same period as the OBS observations via the Incorporated Research Institutions for Seismology (IRIS) Data Management Center (Figure 1a). Most of these onshore broadband stations are located along the Chilean coast between 25 and 55°S. Only a few stations are located in the interior and eastern passive margin, as well as along the coast of Antarctica. Using the data from the OBS array and onshore broadband stations, we measured two types of traveltimes for tomography inversion: absolute P-wave and finite-frequency differential P-wave traveltimes between each station pair. Prior to taking the traveltime measurements, the instrumental response was corrected using Seismic Analysis Code (Goldstein et al., 2003). The resulting seismograms, corresponding to velocity waveforms, had their sampling interval set at 20 Hz.

Absolute P-wave traveltimes were obtained using the Adaptive Stacking method (Rawlinson & Kennett, 2004). In this method, P-wave waveforms were first stacked along the predicted traveltime curve using the seismic velocity model IASP91 (Kennett & Engdahl, 1991) to calculate a reference trace. Subsequently, the alignment of the individual traces and stacked reference trace was iteratively improved by time-shifting each trace to minimize the

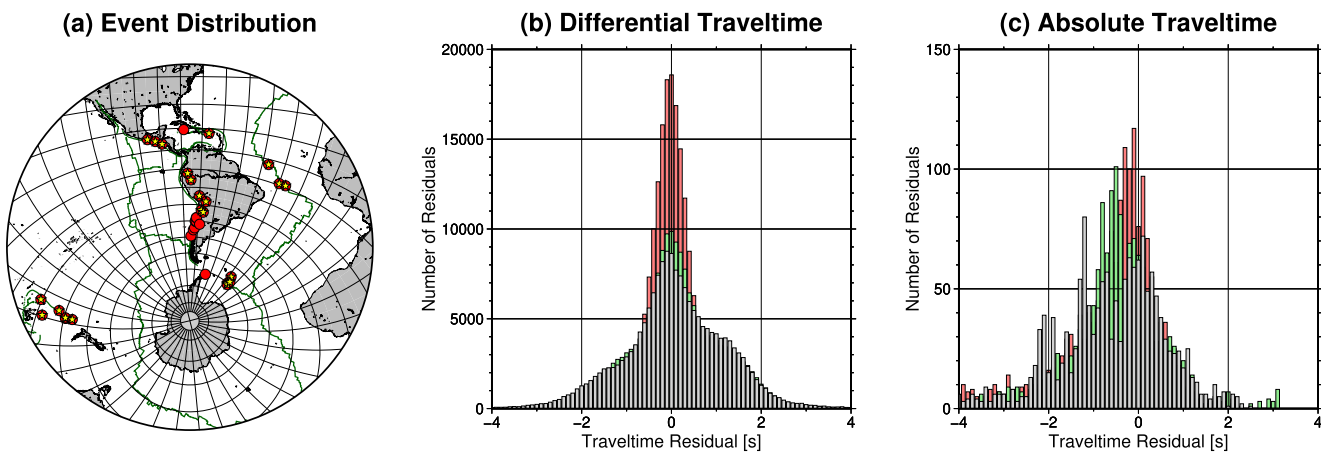


**Figure 2.** (a) Distribution of the seismic events used to measure absolute traveltimes (red circles) and differential traveltimes (yellow stars) within a distance of  $90^{\circ}$  from the OBS array. (b and c) Histograms showing the residuals of measured traveltimes using the theoretical traveltimes calculated with the initial one-dimensional (gray), initial three-dimensional (green), and final three-dimensional (red) velocity models. The total number of (a) relative and (b) absolute traveltimes data are approximately 220,000 and 1,600, respectively.

misfit from the reference trace, leading to an estimation of the residuals from the model prediction. The absolute traveltimes for each station were obtained by adding the time shift of each station from the reference trace to the onset time picked on the high signal-to-noise ratio reference trace. The waveforms were divided into groups by azimuth before being stacked, taking into account the radiation patterns.

Differential traveltimes were measured by cross-correlating band-passed seismograms for all possible station pairs. In this study, we measured the traveltimes for 10 overlapping frequency bands with central periods ranging from 30.0 to 1.4 s. The frequency ranges and estimated measurement errors for each band are summarized in Table S1 of the Supporting Information S1. The differential traveltime is defined as the time shift between band-passed waveforms at which the cross-correlation function achieves the maximum value of the cross-correlation coefficient (Dahlen et al., 2000). The appropriate time windows were set to be sufficiently longer than the center period of each frequency band and to include the manually picked first arrival time. To avoid the influence of the structure difference beneath the stations, we applied crustal corrections to traveltimes between two stations by the cross-convolution of the crustal responses at the two stations following Obayashi et al. (2017) using the crustal model CRUST2.0 (Bassin et al., 2000). Measurements with correlation coefficients of 0.9 or higher were selected and subsequently visually confirmed. We obtained a total of 1,642 P-wave absolute traveltimes for 32 events (Figure 2a) during the OBS observation period and 224,549 P-wave differential traveltimes for 25 events.

In addition to these regional data, global onset times from January 1964 to March 2020, published by International Seismology Centre (2022) (ISC), were obtained (Figure S1 in Supporting Information S1). We extracted events with a magnitude of  $\geq 4.0$  and a number of P observations  $> 50$ , and selected them to be distributed as uniformly as possible in space and time. Traveltimes with residuals of 10 s or more were removed as outliers. Consequently, we obtained 31,011,580 traveltimes for approximately 123,000 events. Measurement errors are assumed to be 0.1, 0.3, and 1.0 s for the traveltimes of iP, P, eP, respectively, according to the ISC's notation. The ISC catalog contains data from short-period seismometers and broadband networks that are not available in the IRIS Data Management Center, resulting in more stations in the eastern region than in the regional array. Prior to the inversion, the traveltime residuals were corrected for topography and ellipticity (Dziewonski & Gilbert, 1976).

### 3. Methods

The tomographic inversion method followed Obayashi et al. (2013) and was based on Inoue et al. (1990). Starting from the initial model, the following steps were repeated until convergence was achieved: (a) relocation of all events; (b) calculation of traveltime residuals; (c) back-projection of traveltime residuals to the slowness perturbation model; and (d) refinement of the one-dimensional velocity model by spherical averaging of the slowness perturbations.

The seismic velocity structure of the entire mantle was parameterized using a block model that divided the mantle into latitudes, longitudes, and depths. The horizontal block sizes varied from  $0.625^\circ \times 0.625^\circ$  to  $5^\circ \times 5^\circ$ , which were determined to ensure that the total length of the rays passing through each block was as uniform as possible. Additionally, the areas bounded by  $30^\circ\text{S}$ ,  $65^\circ\text{S}$ ,  $55^\circ\text{W}$ , and  $80^\circ\text{W}$ , which were the focus of this study, were parameterized with a minimum block size of  $0.625^\circ \times 0.625^\circ$ . The block configuration is illustrated in Figure S2 of the Supporting Information S1. In the radial direction, the mantle was divided into 32 layers with thicknesses of 12, 68, and 334 km at the surface, uppermost, and bottom layers, respectively. The two layers with a thickness of  $\sim 30$  km from the surface were solved as terms for the crustal and station corrections (Figure S4 in Supporting Information S1).

The initial three-dimensional P-wave velocity model was calculated by the tomographic inversion of first arrival time data from 1964 to 2020 obtained from the ISC, described in the previous section. We obtained the initial one-dimensional model by spherical averaging of the initial three-dimensional structures (Figure S5 in Supporting Information S1), which is used for ray-tracing and the calculation of the finite-frequency sensitivity kernels. Figures 2b and 2c show the traveltimes residuals of the regional data sets, when compared to the theoretical traveltimes for the initial one-dimensional, initial three-dimensional, and final three-dimensional velocity models after inversion. All the events were then relocated with respect to the initial three-dimensional velocity model using the same traveltime data as the tomographic inversion. Hypocenter parameters shifted by approximately 10 km horizontally and 15 km in depth in average. This procedure is intended to account for the influence of three-dimensional structure on the event location. After relocation, traveltime residuals were calculated and back-projected onto the mantle as a slowness perturbation. In this study, we used an inversion technique combining methods based on conventional ray theory (Inoue et al., 1990) and finite-frequency theory (Dahlen et al., 2000; Hung et al., 2000). The former approximates seismic waves with infinite frequency, whereas the latter considers frequency-dependent scattering and diffraction and therefore valid for smaller inhomogeneities. In the ray-theoretical method, the traveltime residual  $\delta T$  is a linear integral along the ray  $l$  as follows:

$$\delta T = \int \Delta s dl \quad (1)$$

where  $\Delta s$  is the slowness perturbation. Because  $\delta T$  is sensitive to only velocity heterogeneity along the ray path, the computational cost is very low. In contrast, finite-frequency theory gives traveltime residuals as a three-dimensional volume integral as follows:

$$\delta T = \iiint \frac{\Delta s}{\bar{s}} K dq_1 dq_2 dl \quad (2)$$

where  $q_1, q_2$  are the coordinates perpendicular to the ray path.  $K$  is the finite-frequency sensitivity kernel, which represents the sensitivity of the  $\delta T$  to three-dimensional mantle structure  $\Delta s/\bar{s}$ . This finite-frequency sensitivity kernel has a “Banana–Doughnut” shape: sensitive in a region surrounding the unperturbed ray path and insensitive on the ray. Because the width of the sensitivity kernel depends on the wave frequency, this method can constrain the size of heterogeneity using traveltime data measured in different frequency bands. The differential traveltime residual is as follows:  $\delta(\Delta T) = \delta(\Delta T_B - \Delta T_A)$ , where  $\Delta T_A$  and  $\Delta T_B$  are traveltime residuals calculated by Equation 2 at different stations  $A$  and  $B$ , respectively. The differential sensitivity kernel  $K^{B-A}$  is the difference between the kernels for individual stations (Hung et al., 2000). In this case, the differential kernel has a strong sensitivity only directly below the station and is unaffected by the structure near the source because the overlapping parts of the two kernels are canceled out by subtraction. Sensitivity kernels were calculated using the method described by Dahlen et al. (2000).

The equation of the back-projection of traveltime residuals in each step of the iterative process is as follows:

$$\begin{pmatrix} \mathbf{G} \\ \mathbf{D} \end{pmatrix} \delta \mathbf{m} = \begin{pmatrix} \delta \mathbf{d} \\ -\mathbf{Dm}_0 \end{pmatrix} \quad (3)$$

where  $\mathbf{G}$  is the data kernel,  $\mathbf{D}$  is the smoothness kernel,  $\delta\mathbf{m}$  is the improvement of the slowness perturbation model vector,  $\mathbf{m}_0$  is the initial model, and  $\delta\mathbf{d}$  is the traveltime residual vector. A first-order smoothness prior was imposed, so the smoothness kernel  $\mathbf{D}$  contains the coefficients for the first derivatives of model parameters. Solving this equation using the least-squares conjugate gradient method yielded a new three-dimensional model. The L2 norm  $\Pi$  to be minimized for Equation 3 is as follows:

$$\begin{aligned}\Pi = & \sum_i \frac{1}{\sigma_i^2} \left( t_i^{\text{obs}} - t_i^{\text{1D}} - \sum_k \Delta s_k l_{ik} \right)^2 + \sum_j \frac{1}{\sigma_j^2} \left( t_j^{\text{obs}} - t_j^{\text{1D}} - \sum_k \frac{\Delta s_k}{s} K_{jk} V_k \right)^2 \\ & + \sum_v \left[ \frac{1}{\sigma_h^2} \left( \frac{\Delta S_\theta}{r \Delta \theta} \Delta m_\theta^2 + \frac{\Delta S_\phi}{r \Delta \phi \sin \theta} \Delta m_\phi^2 \right) + \frac{1}{\sigma_v^2} \frac{\Delta S_r}{\Delta r} \Delta m_r^2 \right]\end{aligned}\quad (4)$$

where  $i$  and  $j$  are the index of residuals and  $k$  is the block index.  $l$  is the length of the ray path segments, and  $V$  is the volume of each block.  $\Delta\theta$ ,  $\Delta\phi$ , and  $\Delta r$  are step widths in latitude, longitude, and the radial direction,  $\Delta S$  is the contact area of the adjacent blocks along the coordinate, and  $\Delta m$  are the differences of adjacent slowness models. There are some prior parameters:  $\sigma_i$  and  $\sigma_j$  are the standard error of  $t_i$ ;  $\sigma_v$  and  $\sigma_h$  are the roughness parameters corresponding to the errors of the vertical and horizontal smoothness. The first and second terms in Equation 4 fit the model parameters to the data using ray and finite-frequency theories, respectively. The third term smooths the model with roughness parameters  $\sigma_v$  and  $\sigma_h$ . The parameters  $\sigma_v$  and  $\sigma_h$  were determined to be 4.0e-2 and 2.7e-2 based on the cross-validation analysis and the trade-off curves between data misfit and regularization (L-curves, Figures S6 and S7 in Supporting Information S1). The residual data sometimes contain large errors, so robust estimation was employed by applying a weight  $w$  as a function of the traveltime residual  $r$  as

$$w = \begin{cases} [1 - (r/10)^2]^2, & |r| < 10 \text{ s} \\ 0, & |r| \geq 10 \text{ s} \end{cases}\quad (5)$$

The ray-theoretical method was applied to the regional absolute traveltimes and onset times from the ISC bulletin, and the finite-frequency method was applied to the differential traveltimes as a function of the frequency. It is technically straightforward to jointly invert finite-frequency traveltime measurements with ray-theoretical arrival times (Montelli et al., 2004). In this study, no weights were assigned between the ray-theoretical kernel and the finite-frequency kernel. Increasing the weight of the finite-frequency kernel tends to increase the variance of both the model parameters and the residuals. In addition, Obayashi et al. (2013) showed that the difference between models obtained using finite-frequency kernels and ray-theoretical kernels was negligible for onset times. Therefore, a high-resolution model can be obtained with a large amount of data while saving computational cost by using the ray-theoretical method for a huge amount of global traveltimes and the banana-doughnut kernel for finite-frequency traveltimes for the target region.

Solving Equation 4 with the least-squares conjugate gradient method yields a three-dimensional model. The one-dimensional model was refined by averaging the slowness perturbation of each layer. The obtained spherically averaged one-dimensional model was then used as the reference model for ray-tracing and data kernel calculation, while the three-dimensional model was used for event relocation in the next iteration step. The roughness parameters were fixed during each iterative inversion. We iterated relocation, ray-tracing, and the calculation of the ray-theoretical and finite-frequency kernels. The final model was achieved after three iterations with RMS converges (Figure S8 in Supporting Information S1).

## 4. Results

### 4.1. Checkerboard Resolution Tests

Checkerboard Resolution Tests were performed to evaluate the resolution of the velocity structure obtained from the data set. To examine the resolutions at different scales, two input models with horizontal pattern sizes of  $2.5^\circ \times 2.5^\circ$  and  $5^\circ \times 5^\circ$  were defined. The pattern changed vertically every three layers. Both input models were given slowness perturbations of amplitude  $\pm 2\%$ . We added a Gaussian noise with a standard deviation of 0.30 s to the synthetic traveltime data.

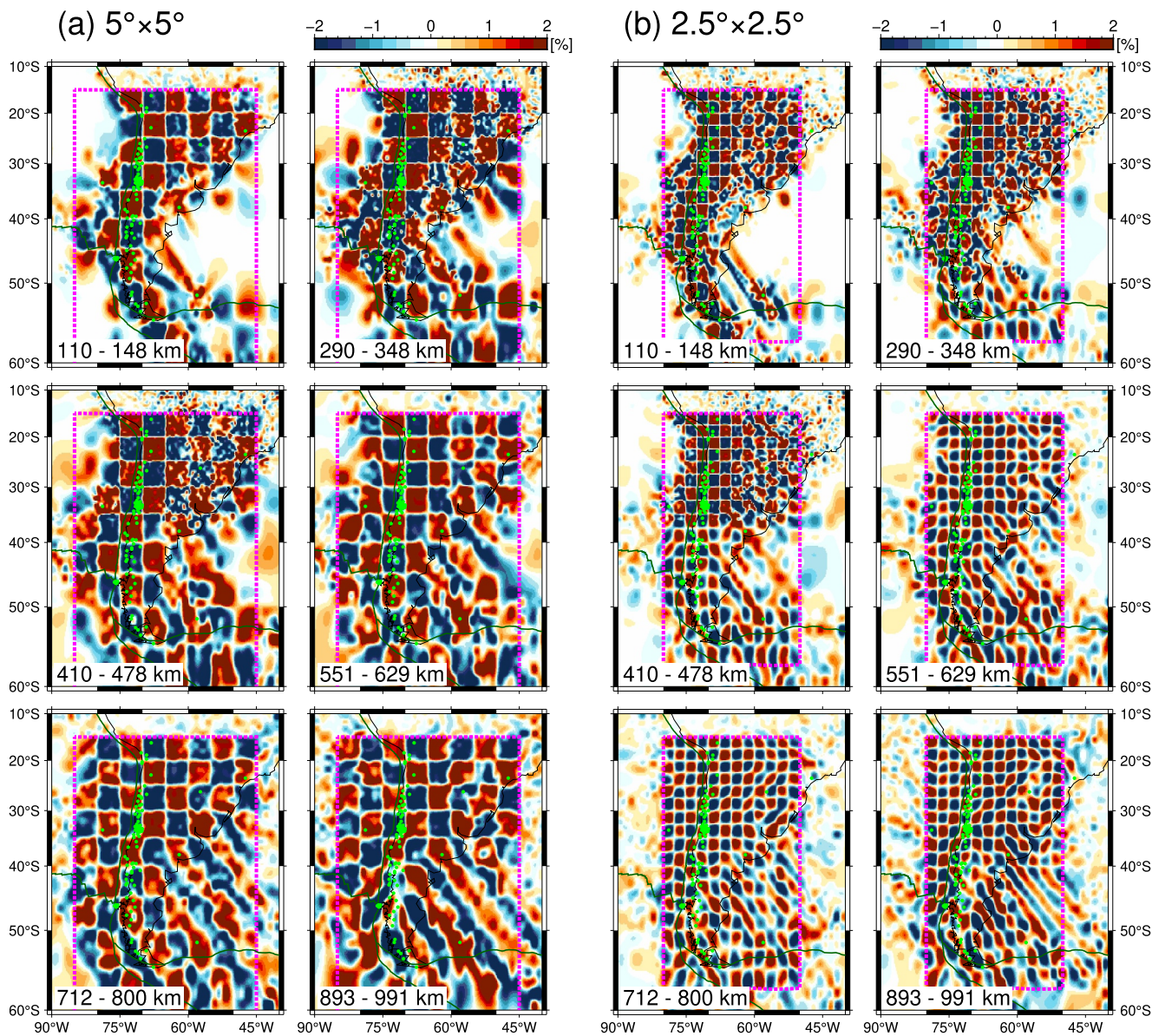


**Figure 3.** Output models for checkerboard resolution tests using (a)  $5^\circ \times 5^\circ$  and (b)  $2.5^\circ \times 2.5^\circ$  patterns of slowness perturbations with an amplitude of  $\pm 2\%$ . The green dots denote seismic stations and plate boundaries are represented by dark-green lines. The slowness anomaly is presented as a percentage deviation from the one-dimensional initial velocity model. The initial checkerboard pattern was placed within the area defined by the dotted magenta line.

The outputs for the long-wavelength structure with  $5^\circ \times 5^\circ$  checkers showed that the pattern was well recovered in the continental region down to a depth of approximately 1,200 km (Figure 3a). The input anomaly amplitudes ( $\pm 2\%$ ) were fully recovered from above the transition zone to approximately 1,000 km depth, indicating a good amplitude recovery within this depth range. The high-resolution region where input anomalies were well reconstructed was along the west coast at a shallow depth of 110–150 km, and extended east and west with depth. The  $5^\circ \times 5^\circ$  pattern was well reconstructed on the South American continent below a depth of 300 km. Smearing artifacts, elongated in a northwest to southeast direction, were observed in the southeast area. Reconstruction of the  $2.5^\circ \times 2.5^\circ$  pattern indicated that the structures beneath the western part of the continental region were well resolved (Figure 3b). The patterns did not recover well south of  $\sim 45^\circ\text{S}$  and deeper than 800 km compared to the long-wavelength case. These results indicate that our model resolves velocity inhomogeneities greater than 250 km under the continent at depths of up to  $\sim 800$  km.

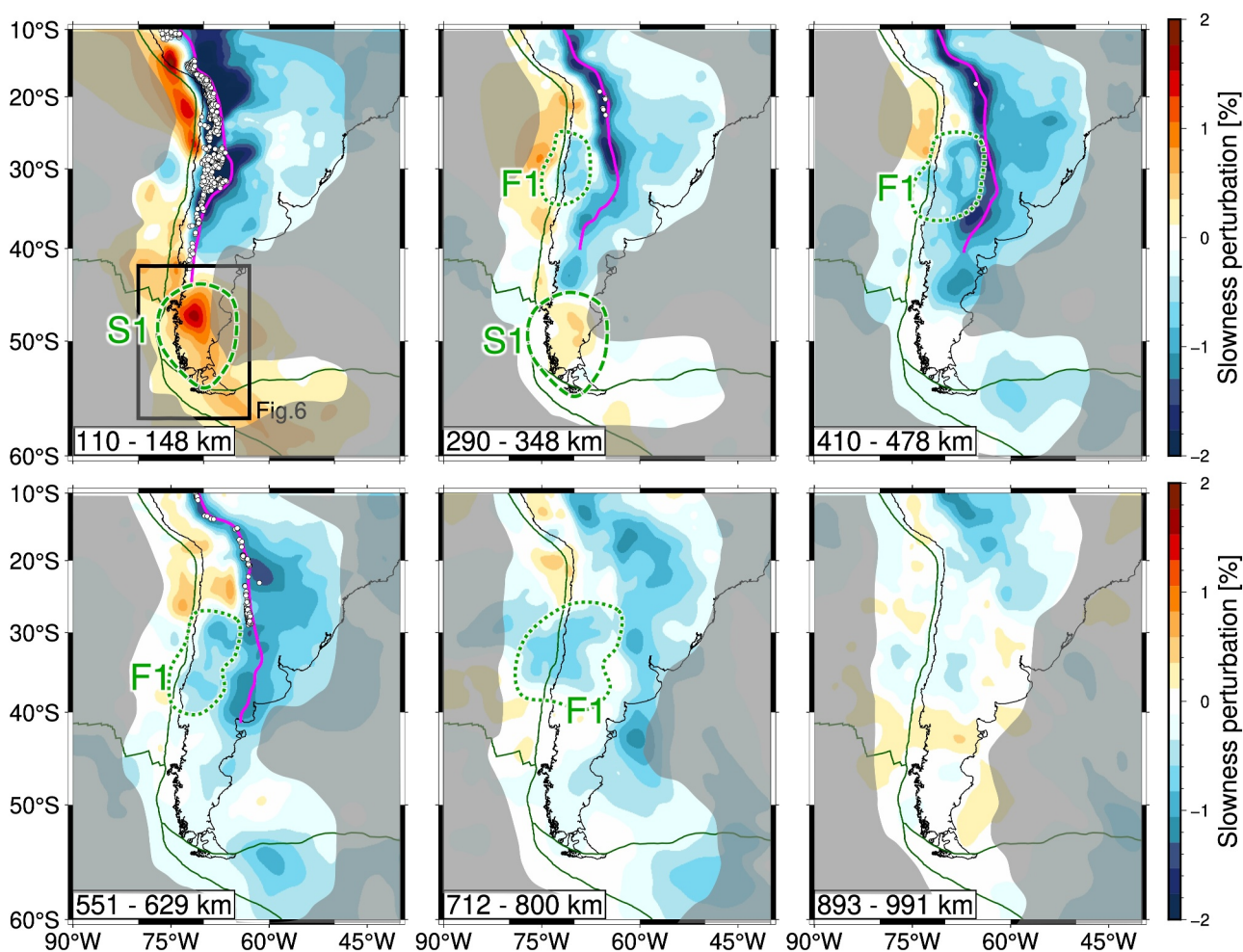


**Figure 4.** Depth slices of our final tomography model up to approximately 1,000 km depth. The red color indicates slower seismic velocities relative to the spherically averaged seismic velocity at each layer, while blue denotes faster velocities. Detailed, enlarged views of the vicinity of the CTJ are shown in Figure 5. Event hypocenters within each depth layer are marked with white dots. The contour of the Nazca slab by the Slab2 model (Hayes et al., 2018) is denoted by magenta lines. The poorly resolved areas, based on the checkerboard resolution tests and ray path density, are masked with gray. Anomalies labeled “F1,” and “S1” are discussed in the text.

#### 4.2. Tomography Model

The horizontal and cross sections of our final tomography model are shown in Figures 4–6. These figures represent slowness perturbations in percentages, which are the residuals of the average slowness at each depth layer divided by the spherical average slowness. Compared to the initial model derived from only global ISC traveltimes data, the final model shows a more detailed structure from 25 to ~55°S with the contribution of the additional measured traveltimes data (Figure S9 in Supporting Information S1).

The most notable structure in the northern part is the fast anomalies extending in a north-south direction. These fast anomalies are consistent with the Wadati–Benioff zone in the upper mantle and the geometry of the Chile Trench and thus can be interpreted as the subducted Nazca slab. In the upper mantle, the Nazca slab anomaly is relatively narrow, with a horizontal width of less than 200 km perpendicular to the trench. Up to a depth of 1,000 km, the slab was continuously observed as a region where the negative slowness perturbation was approximately 0.65% or stronger. These anomalies shift eastward with increasing depth and can be interpreted as cold lithospheric subduction at a certain dip angle. In the upper mantle at 32–40°S, the fast anomaly is weakened (Figures 6c–6e). Portner et al. (2017) detected a hole of several hundred kilometers in diameter in the Nazca slab at depths of 200–400 km around 32°S, and slow anomalies linked to sub-slab slow anomalies are also found in the hole. They proposed that buoyancy contrast in the slab caused the hole, allowing sub-slab material to rise into the mantle wedge. The slab hole and slow anomalies here are also supported by Rodríguez et al. (2020) and Lynner et al. (2017). In our results, the

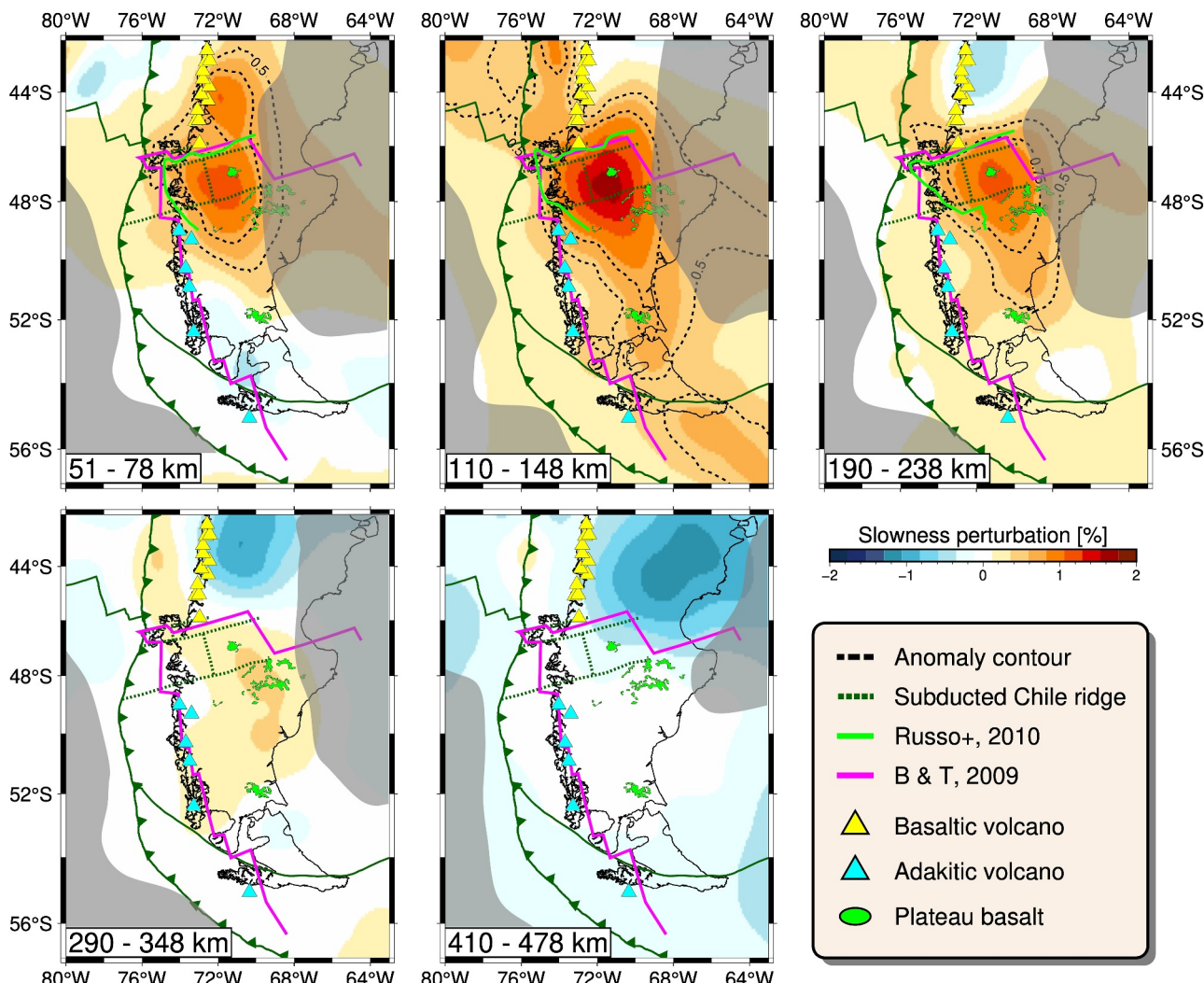


**Figure 5.** Resultant model focusing on the vicinity of CTJ (black line area in Figure 4). The black dotted lines indicate contours of a slow anomaly stronger than 0.5% in the model, with 0.25% increments. The geometry of the Chile Ridge and associated fracture zones are projected to depth, as shown by dark-green dotted lines. Previously estimated slab windows, according to Russo et al. (2010) and Breitsprecher and Thorkelson (2009), are included for comparison.

amplitude reduction of the slab high-velocity anomaly along profile c is spatially consistent with this hole, but without significant low velocities. However, our model was not capable of distinguishing them, as shown by the results of the synthetic recovery tests in the next section. The pattern of slab subduction varied significantly along the trench. At latitudes of 20–26°S, the slab subducts at a constant dip angle (approximately 15°–20°) from the Chile Trench to the mantle transition zone and is stagnant horizontally for more than 1,000 km in the mantle transition zone. In contrast, in the range of 28–32°S, the slab lies horizontally for more than 300 km, at a depth of approximately 130 km, and then abruptly subducts with a larger dip angle. Further south, no slab bending associated with flat subduction was observed. These features are consistent with those of previous studies on the Nazca slab geometry (Ciardelli et al., 2022; Mohammadzaheri et al., 2021; Portner et al., 2020).

Two prominent strong anomalies were observed around the subducted Nazca slab: (a) fast anomalies beneath the Nazca slab at depths of 300–800 km between 26 and 35°S (F1 in Figure 4) and (b) strong slow anomalies on the eastern side of the CTJ (S1 in Figure 4). The F1 anomalies are approximately parallel to the bottom of the Nazca slab; however, the deeper and southern parts of the F1 anomalies approach the Nazca slab, and their separation becomes unclear. The amplitude was less than that of the Nazca slab anomaly at all depths, with a maximum amplitude of 1.06% at the top of the mantle transition zone at 28.5°S. In the upper part of the transition zone, F1 extended 800 km along the trench direction, with an approximate width of 300 km. It extended to the south,

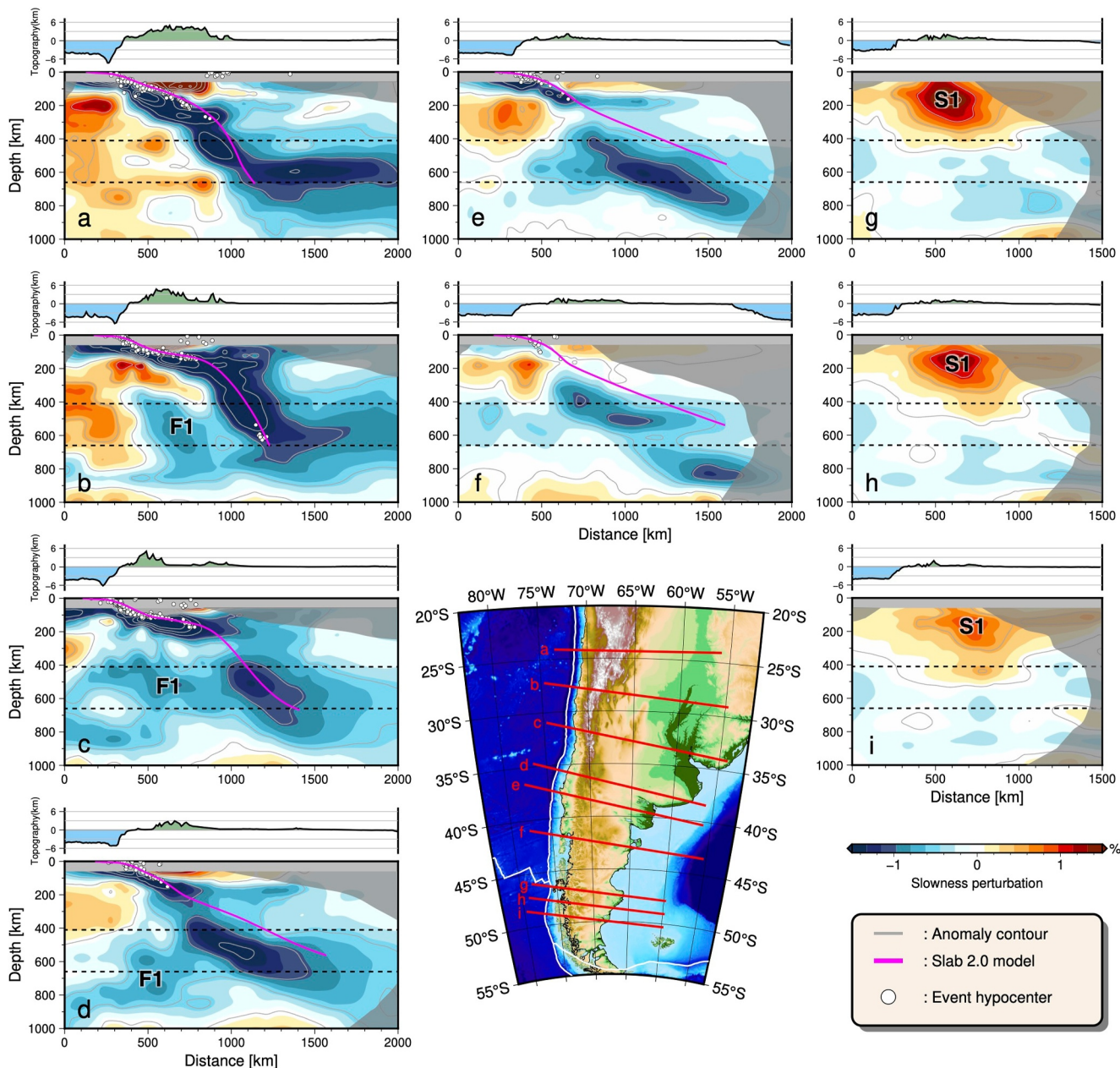


**Figure 6.** Cross sections of the resulting model approximately perpendicular to the trench strike along profiles (a–i) which are delineated in the map. Two black dashed lines represent the 410 and 660 km seismic discontinuities, respectively. White dots denote the hypocenters of the seismic events. The top surface of the subducting Nazca slab of the Slab2 model (Hayes et al., 2018) is denoted by magenta lines. The topography along the profile is shown above each cross section. Anomalies “F1,” and “S1” are labeled and discussed in the text.

reaching a north-south length of 1,200 km just below the transition zone. These large fast anomalies have been observed in prior teleseismic studies, with amplitudes equal to or slightly weaker than those of the Nazca slab (Pesicek et al., 2012; Portner et al., 2020), but there are discrepancies in their distributions. Pesicek et al. (2012) observed weak (~1.0%) fast anomalies from 37 to 40°S at depths ranging from 200 to 800 km, whereas Portner et al. (2020) showed strong (~2.0%–3.0%) fast anomalies from 24°S (depths of 300–800 km) to 38°S (depths of 500–1,000 km).

In the vicinity of the CTJ, notably slow anomalies (S1 in Figures 4 and 6g–6i) were observed, with a maximum perturbation of 1.6% at ~48°S in a depth slice of 110–148 km. These anomalies were bounded on the west side by the trench and extended southeast to 54°S with a gradually decreasing amplitude. The region of strong anomalies

shifts eastward with depth, suggesting that S1 dips eastward. S1 was observed continuously up to a depth of 350 km. Based on its location, S1 can be interpreted as a slow anomaly associated with the Patagonian slab window. S1 is generally consistent with previous studies of regional teleseismic P-wave tomography near the CTJ (Miller et al., 2023; Russo et al., 2010) and a recent Rayleigh wave dispersion analysis (Mark et al., 2022). Active adakitic volcanism (Stern & Kilian, 1996) is located at the southern edge of S1. As noted above, the Nazca slab, which was expected to be on the north side of the slab window, was imaged as a less anomalous region surrounded by slow anomalies to the west and south. The southern side of S1 (48–52°S), the Antarctic slab, which is expected to exist up to a depth of 45 km (Breitsprecher & Thorkelson, 2009), was not clearly represented in the resulting velocity model. Although weak fast anomalies were observed at a depth of 50 km, we did not interpret them because of low ray path coverage and weak amplitude.

In addition, there are slow anomalies on the western side of the slab between 20 and 32°S above the mantle transition zone (Figures 4 and 6b). The location of these slow anomalies is generally consistent with Portner et al. (2017), who interpreted the slow anomalies as a warm asthenospheric mantle derived from a hotspot entrained by the Nazca plate motion, although the anomalies were weaker and narrower. This anomaly extends north of the northern limit of the study area, 25°S, therefore a detailed discussion would require extending the study area further north.

#### 4.3. Synthetic Recovery Tests

In addition to checkerboard resolution analysis, we performed synthetic recovery tests in which synthetic structures were reconstructed to examine how well the given structures were recovered using the data set used in this study. Synthetic P-wave traveltimes and differential traveltimes of all event-station pairs used in the tomographic inversion were calculated for the given test structures and then inverted to recover the test model. This test was applied to assess the reliability of three notable structures: the Nazca slab, the subslab fast anomaly (F1), and the slow anomaly associated with the Patagonian slab window (S1).

The first synthetic recovery test was conducted on the Nazca slab. Based on the resulting velocity model, we constructed synthetic fast anomaly structures for the Nazca slab, in which a uniform fast anomaly of 2% was given. The recovered model is shown in Figure 7a. The geometry of the fast anomalies in the recovered model was in accordance with that of the test model, although the recovered intensity varied regionally. North of 30°S, approximately 100% of the amplitude of the input slab model was recovered at all depths. South of 30°S, the recovered amplitude was smaller than that of the input model at a depth range of 200–400 km and in the lowermost mantle transition layer. The results of the test suggest that the configuration of the Nazca slab north of 30°S is well-constrained. Weak, slow anomalies appeared around the slab, indicating that caution should be exercised when interpreting low-velocity anomalies with small amplitudes around slabs.

Because the reconstruction model of the Nazca slab showed the weakening of the fast anomaly south of 30°S at the depth of around 300 km, this weakening, which was observed in the resulting model (Figures 6c–6e), was additionally tested (Figure S10 in Supporting Information S1). We altered the amplitudes of anomalies in the input model within the 2° north-south range from each profile at a depth range of 250–400 km. For inputs with a slab hole, the hole was filled by weak fast anomalies due to smearing from upper and lower layers. These results indicate that the weakening of the fast anomaly slab in the resulting model cannot be determined to be caused by the presence of the hole of several hundred kilometers in size. Furthermore, the slow anomaly in the hole at 32°S (profile c) indicated by Portner et al. (2017) was tested with an input model in which the hole was filled with 2% slow anomaly. The model was reconstructed as a hole with a slightly fast anomaly rather than the slow anomaly, suggesting that it is not possible to determine whether a hole or a slow anomaly exists.

Another synthetic test was performed to examine the resolution of the subslab fast anomalies (F1). The input model was constructed by adding fast subslab anomalies to the synthetic Nazca slab used in the previous recovery test. We tested two different subslab fast anomalies with amplitudes of 2%, the same as those of the synthetic Nazca slab, and additionally 1% (Figures 7b and 7c, respectively). In both cases, the shape and amplitude of the input subslab anomalies were recovered well, indicating that the intensity of the F1 anomalies was significantly lower than that of the Nazca slab at the same latitude. Slow anomalies appeared between the Nazca slab and F1 in the recovered models, suggesting that those in the resulting model could be artifacts. The extension of the fast anomalies associated with the slab and F1 anomaly across the 660-km discontinuity into the uppermost lower

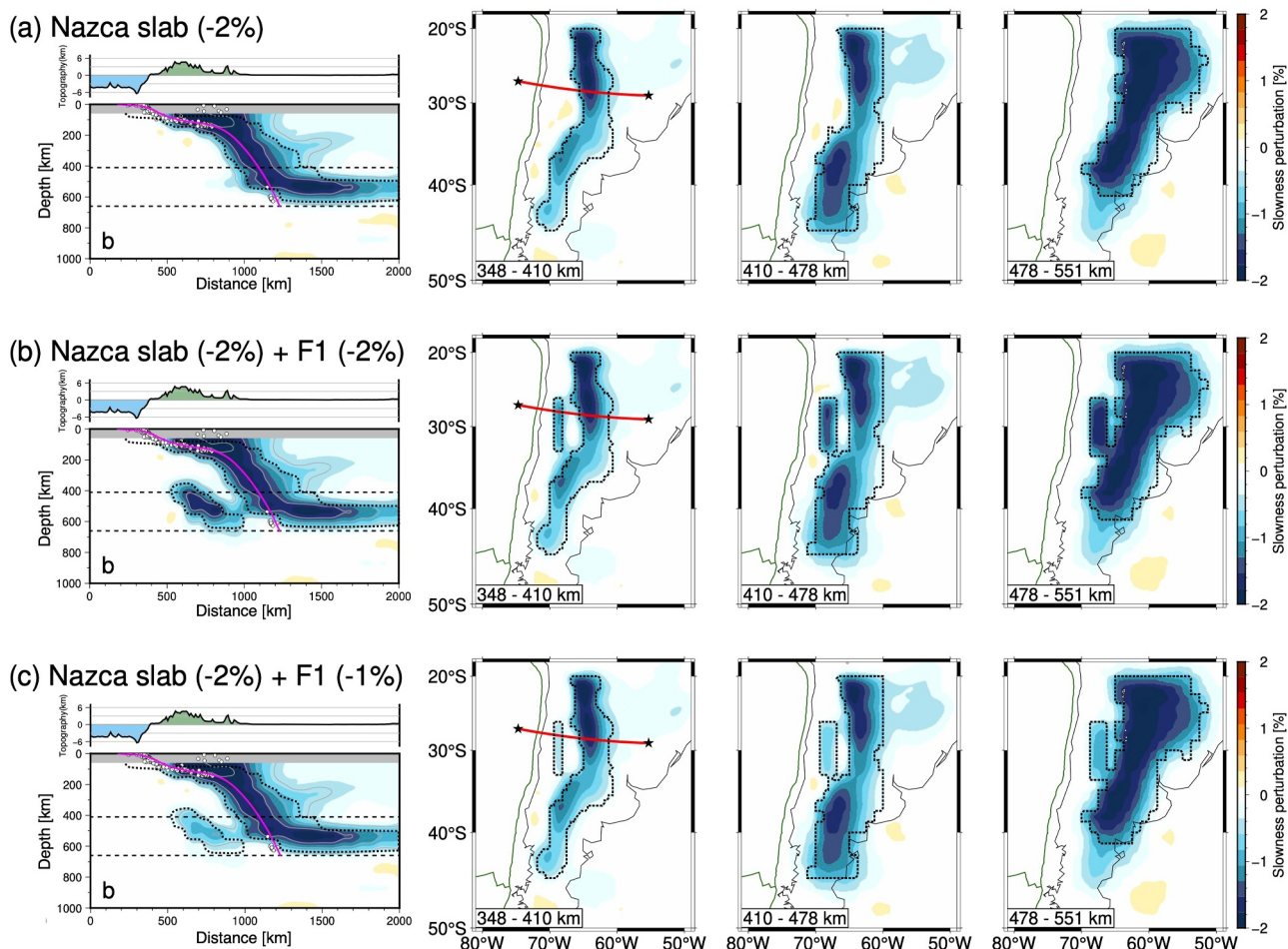


**Figure 7.** Results of synthetic anomaly recovery tests for Nazca slab and subslab fast anomalies. The traces for cross sections are same as in Figure 6b and shown as a red line in the left map. These tests are for (a) Nazca slab anomaly (2%), (b) Nazca slab anomaly (2%) with F1 anomaly (2%), and (c) Nazca slab anomaly (2%) with F1 anomaly (1%). The dotted black line outlines the input anomalies. Other cross sections and additional synthetic recovery tests are shown in Figures S10 and S11 of the Supporting Information S1.

mantle was also verified by synthetic recovery tests and confirmed to be reliable (Figure S11 in Supporting Information S1).

Synthetic recovery tests were also conducted on slow anomalies associated with the slab window. The synthetic slab window was defined based on areas with slowness perturbations greater than the thresholds in each layer in the resulting model (0.7% in the shallowest layer and 0.3% in the deepest layer at a depth of 350 km) and assigned a slow anomaly of 3%. To assess the depth of the slow anomalies, we created three input models with different bottom depths for the slow anomalies (approximately 150, 240, and 350 km). The recovered models showed a smearing of up to two layers below the bottom of the given slow anomalies in all cases, indicating that the actual vertical extent of the structure could be shallower than the deepest layer of the resulting model (Figure 8). Our final tomographic model best matched the model recovered from input anomalies down to 240 km. In addition, the horizontal spread of the slow anomalies was tested using two different input models (Figure S13 in Supporting Information S1). One was the maximum distribution, based on the slab window predicted by the plate reconstruction model (Breitsprecher & Thorkelson, 2009), and the other was the minimum extent, based on a slow area at a depth of 110 km in the resulting velocity model. The amplitude of the input velocity anomaly was 3% in both cases. The western and north-south extents were well constrained for the most part, but the eastern edge could not be constrained because of the lack of stations.

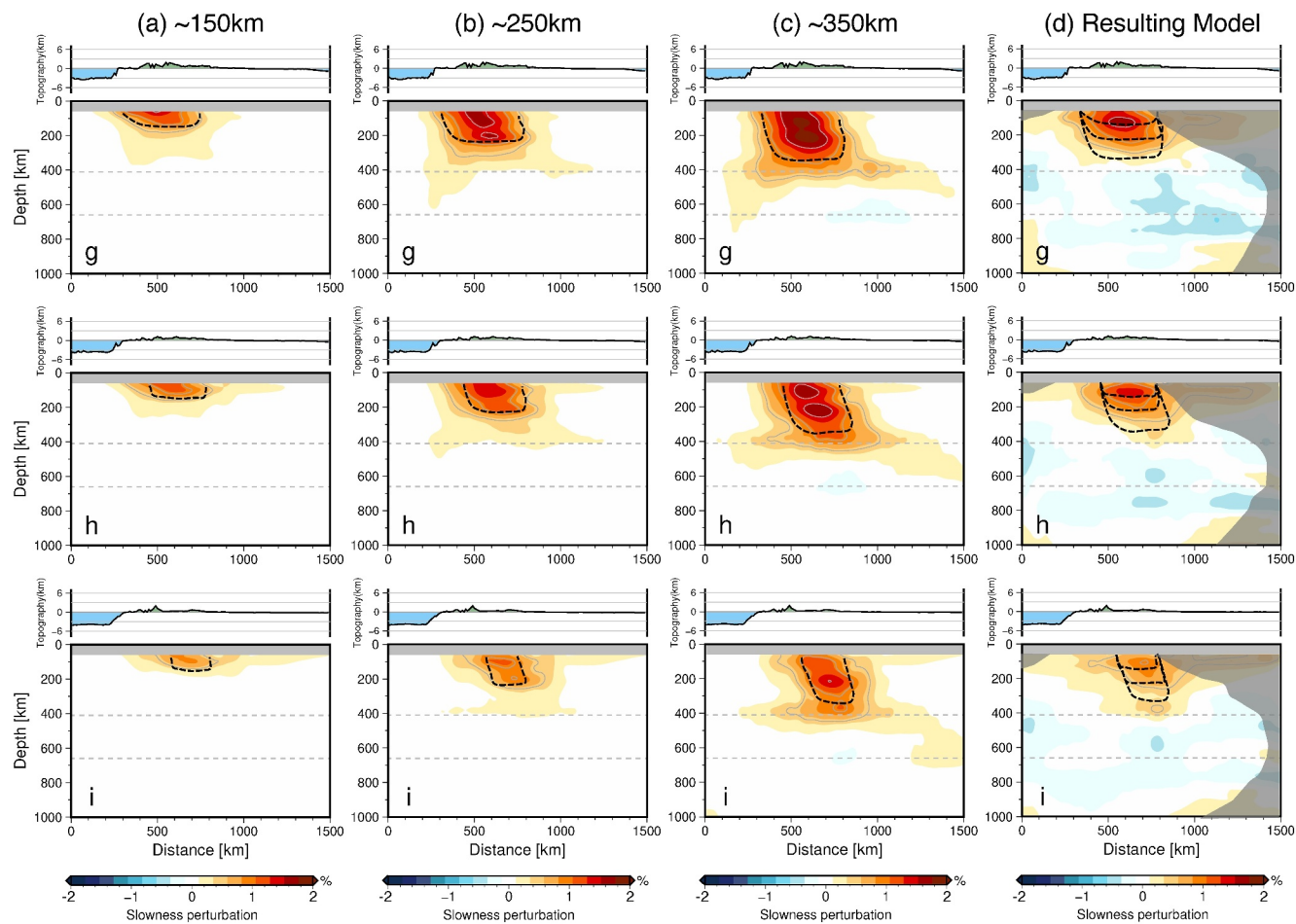


**Figure 8.** Results of synthetic anomaly recovery test for the vertical smearing of S1 anomaly for alternating depth layers along (g–i) in the map in Figure 6. Tests are performed on slow anomalies with an amplitude of 3% up to a depth of approximately (a) 150 km, (b) 250 km, and (c) 350 km. The dashed black line outlines the input anomaly. (d) For comparison, the final tomography model is shown in the same cross sections. The horizontal slices at different depths and the corresponding synthetic recovery test are shown in Figures S12 and 13 of the Supporting Information S1, respectively.

## 5. Discussion

### 5.1. Model Comparison With Previous Tomographic Studies

The final model was compared with depth slices of global and regional P wave tomography models (Figures 9 and 10). GAP\_P4 (Obayashi et al., 2013) is our previous global model that uses first arrival times in the ISC-EHB catalog between 1964 and 2008, onset times picked on broadband seismograms in the western Pacific, China, Japan, and Australia, as well as PP-P differential time data from the IRIS broadband seismic network and finite-frequency relative P-wave traveltimes between stations in the western Pacific and Eurasian Russia. DETOX-P1 (Mohammadzaheri et al., 2021) used ISC-EHB catalog data from 1967 to 2014 and finite-frequency traveltime measurements from broadband seismograms from various networks accessible through the FDSN, including the IRIS DMC, European data centers, and regional centers from 1990 to 2016. LLNL-G3Dv3 (Simmons et al., 2012) includes traveltimes from the LLNL database, which includes ISC-EHB and NEIC bulletins, as well as data from Peaceful Nuclear Explosions (PNE) seismic deployments, large refraction surveys, the USARRAY Transportable Array (TA), and temporary PASSCAL deployments worldwide. SAM5\_P\_2019 (Portner et al., 2020) integrates finite-frequency relative traveltimes from 42 seismic networks across South America, including both permanent and temporary portable seismic deployments. This model shows smaller patch-like anomalies with larger amplitudes than the other models, which possibly reflects their relatively weak smoothing and weak damping.

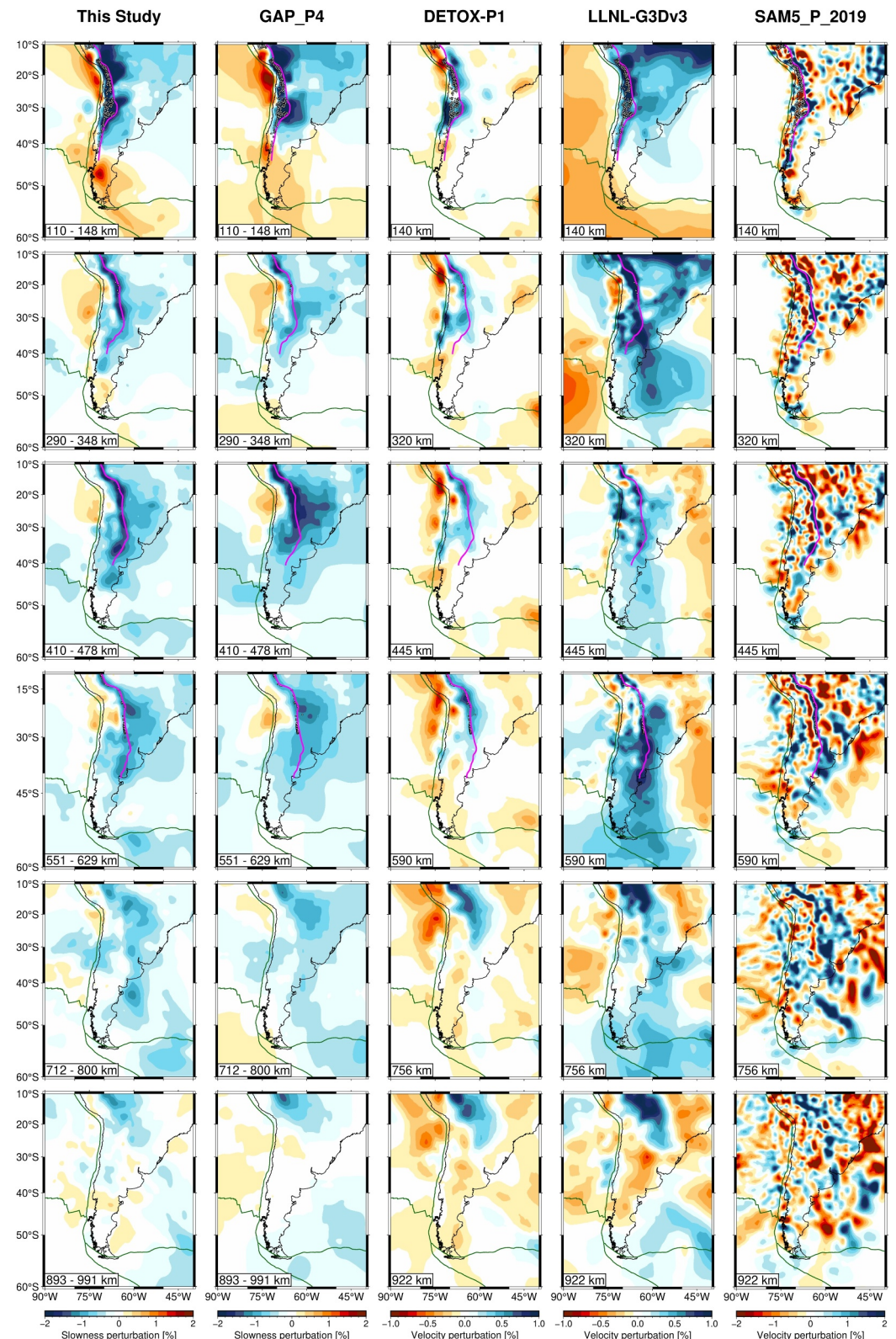


**Figure 9.** Model comparison with existing global and regional tomographic studies. Our model is shown in depth slices (left column) in comparison to global P-wave tomography models GAP-P4, DETOX-P1, LLNL-GsDv3, and regional model SAM\_P\_2019. Note the different color scales for each model. The notations of each panel follow Figure 4.

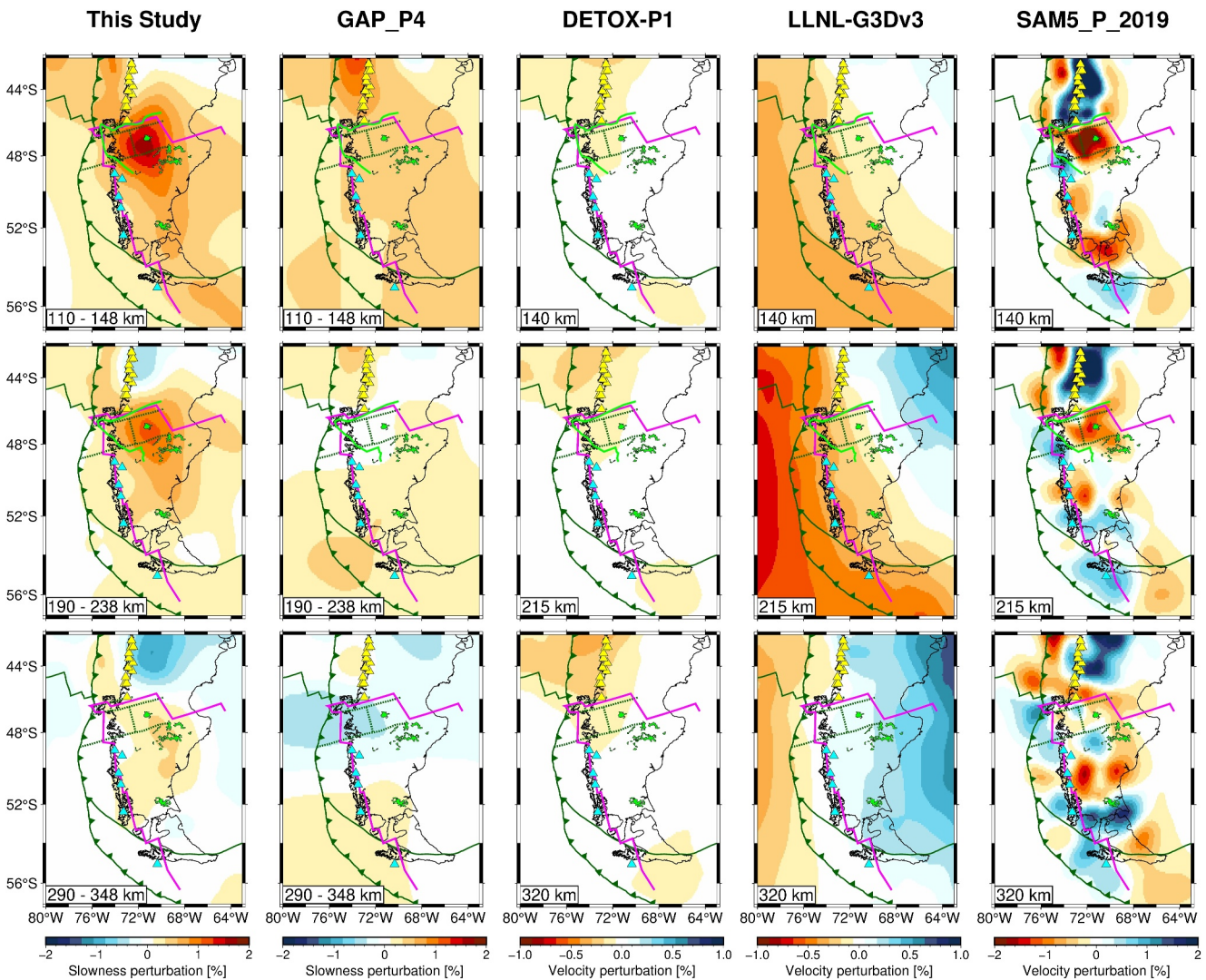


**Figure 10.** Model comparison around the CTJ. Same as Figure 9, but the notations follow Figure 5.

To the north of  $25^{\circ}\text{S}$ , a continuous slab geometry extends into the lower mantle, which is consistent across all models. In contrast, the structures differ among the models to the south of  $30^{\circ}\text{S}$ , where our measured traveltimes data are distributed. For instance, there are discrepancies in the presence and configuration of fast slab anomalies among the models, especially between  $40$  and  $45^{\circ}\text{S}$ . At a depth of around  $320$  km, our model and SAM5\_P\_2019 show a high-velocity anomaly connected to the northern slab, while other models either do not show it or show a slow anomaly instead. The location of fast anomalies within and just beneath the mantle transition zone also varies among the models, suggesting that the penetration of the Nazca Slab into the lower mantle is still controversial. The distribution and amplitude of the slow anomalies generally show large differences between the models, indicating that the slow anomalies are relatively difficult to resolve. The slow anomalies on the western side of the subducting plate are generally observed. However, there is little agreement on their extent, except for the region around  $300$  km depth at  $\sim 20^{\circ}\text{S}$ . All models suggest the presence of F1, a fast anomaly isolated from the Nazca Slab, but its distribution varies among models. The anomaly corresponding to the slab and F1 appears smeared together in GAP4 and DETOX-P1, while the F1-like anomalies are well separated from the slab and have a large amplitude in LLNL-G3Dv3 and SAM5\_P\_2019. Further discussion requires data correction from short-period and temporal seismic stations and use of the later phases. The slow anomalies to the east of the CTJ are not observed since the resolutions of the global model in the region are low due to lack of regional data in the southernmost part of South America. In SAM5\_P\_2019, there is a low-velocity anomaly on the east side of the

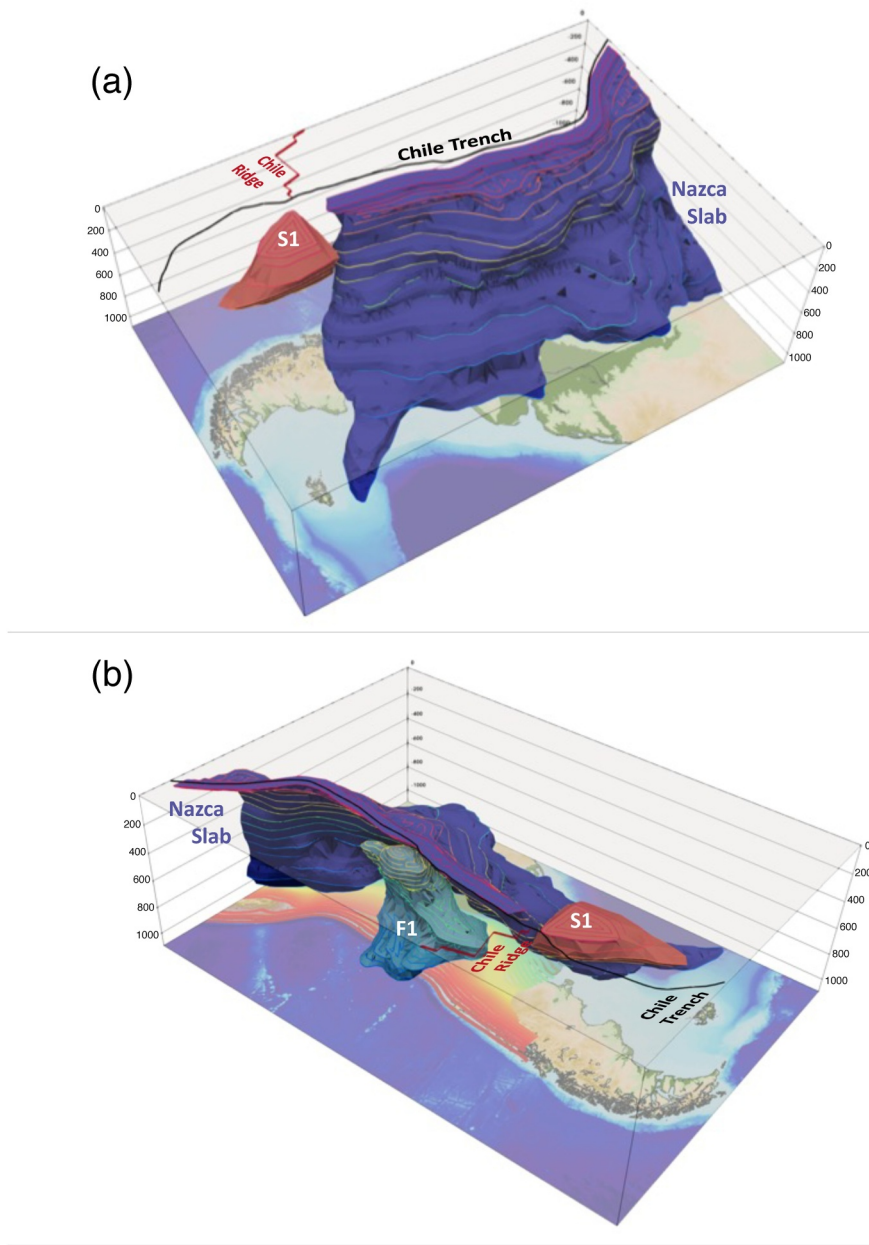


**Figure 11.** Schematic cartoon summarizing our main findings. (a) Southeastern view and (b) southwestern view of the illustration of the subducting Nazca slab and two prominent velocity anomalies interpreted in this paper. The image illustrates the interpreted Nazca slab in dark blue, the fast velocity anomaly F1 beneath the Nazca slab in light blue, and the slow velocity anomaly S1 to the east of the CTJ in red.

CTJ. Although Portner et al. (2020) did not mention this feature because it is shallower and further south than their interest, their image is in good agreement with our model.

### 5.2. Subslab Fast Anomaly Beneath the Nazca Slab

An evident high-velocity anomaly (F1) was observed beneath the Nazca slab between 26 and 35°S (Figures 4, 6b–6d, and 11b). F1 is isolated from the Nazca slab fast anomaly and extends to depths of 300–900 km between the latitudes of 26–33°S, where the flat Nazca slab is located, although it approaches the Nazca slab southward. South of 33°S, in the region of normal Nazca slab subduction, F1 is situated in and below the transition zone and gradually becomes one with the Nazca slab. The amplitudes of the F1 anomalies were smaller than those of the

Nazca slab anomalies over the entire F1 range. Such fast anomalies beneath the Nazca slab have been observed in previous global and regional tomographic studies, albeit with varying sizes, geometries, and amplitudes (Amaru, 2007; Li et al., 2008; Mohammadzaheri et al., 2021; Pesicek et al., 2012; Portner et al., 2017; Scire et al., 2017; Simmons et al., 2012).

Recently, several interpretations have been proposed for the F1-like fast anomalies. Rodríguez et al. (2020) found a fast anomaly beneath the Chile Trench in the latitude range of 25–35°S, with a depth of 200–1,000 km, using teleseismic shear wave tomography, and attributed it to a remnant of the Phoenix slab that was detached and stagnated in the mantle transition zone. Gao et al. (2021) estimated the S-wave velocity structure in the upper mantle through full waveform inversion and detected a high-velocity anomaly at a depth range of 200–350 km at locations similar to F1. They interpreted this anomaly as a fossil fragment of the Nazca slab that subducted steeply before the onset of flattening. They also argued that it is not appropriate to interpret this anomaly as a relic of the Phoenix plate, which was completely subducted by the Late Cretaceous (Gianni et al., 2018; Horton, 2018). Our model suggests that F1 corresponds to a detached segment of the Nazca slab associated with flat slab subduction for several reasons discussed below.

The range of F1 values observed in the resulting model was in good agreement with the locations of the current and past flat-slab segments. The northern edge of F1 (~26°S) is consistent with the Pampean flat-slab segment, which has been flat since 12 Ma when the Juan Fernández Ridge was started subducting (Horton, 2018). South of the current Pampean segment, the magmatic distribution, tectonic evolution, and structure of the overriding plate indicate that flat-slab subduction (Payenia flat slab) occurred from 13 to 5 Ma but is currently subducting relatively steeply (Ramos & Folguera, 2009). Although the eastern edge of the current downgoing slab in this region is still debated, it is continuous to at least ~60°W in our resulting model. The coincidence of the locations between the F1 anomaly and flat slabs indicates that the F1 anomaly may have been the relic Nazca slab that detached when slab flattening occurred (12–13 Ma).

Slab break-off associated with the flat-slab subduction process has been debated in geodynamic models for both steep-to-flat (e.g., Axen et al., 2018; Liu & Currie, 2016, 2019) and flat-to-steep (e.g., Dai et al., 2020) transitions. In the case of a steep-to-flat transition, assuming that flat subduction originates from the trench-forward fast migration of the overriding continental plate and the subduction of a buoyant oceanic plateau, the oceanic lithosphere on the continental side is under tensional stress owing to the competing effects of the dense slab and buoyant oceanic plateau. This extensional stress can lead to slab break-off, in which a dense slab segment is detached. After the break-off of a dense slab, the oceanic lithosphere with a buoyant plateau is deflected upward to a sub-horizontal position near the base of the continental lithosphere (Liu & Currie, 2016). Flat-slab subduction is generally unstable and eventually transitions to normal (steep) subduction via slab rollback or delamination (Dai et al., 2020). Slab rollback or delamination can occur if the slab becomes denser due to eclogitization after it has existed for a sufficient time at suitable pressures and temperatures for phase change. Additionally, the partial eclogitization of an oceanic plateau before or after flat subduction may play an important role in the sinking of broken-off slab segments and their timing (Arrial & Billen, 2013; Liu & Currie, 2016, 2019).

If the slab break occurred at the beginning of the slab flattening at the Pampean and Payenia (12–13 Ma), the Nazca slab should be at least as long as the length of the slab that has been subducted since this flattening. The paleo-convergence rate between the Nazca and South America plates is estimated to be 10–12 cm/yr for the period 25–5 Ma (Cande & Leslie, 1986), while the current convergence rate is ~7 cm/yr (DeMets et al., 2010). Assuming these convergence rates, the slab length, subducted for 13 Myr, is 1,150–1,310 km. These values are not significantly different from the ~1,500 km long fast anomalies of the Nazca slab extending from the Chile Trench to the mantle transition zone in our model. Furthermore, the South American trench has been retreating westward over a long period, and the reconstruction model suggests that it has retreated  $240 \pm 50$  km since 12 Ma (Liu & Currie, 2019; Schepers et al., 2017). Therefore, if the Nazca slab break-off associated with slab flattening occurred near the trench at that time and the detached slab segment subsided vertically, the slab fragment would be expected to be several hundred kilometers east of the present-day trench location. This is consistent with the location of F1 in the model.

However, the temperature difference between F1 and the Nazca slab, which is estimated from the fast anomaly intensities, does not suggest that F1 was caused by slab detachment due to the subduction of the spreading ridge. The history of subduction in this region is associated with complex tectonics, resulting primarily from spreading between the Pacific, Phoenix, Antarctic, and Farallon plates since at least 84 Ma. The Farallon–Phoenix Ridge

began to subduct beneath South America at  $\sim 63$  Ma, although its latitude along the trench is still under debate (Cande & Leslie, 1986). At  $\sim 27$  Ma, the Farallon plate was split into the Nazca and Cocos plates. The Nazca–Phoenix Ridge continues to spread and subduct beneath South America. At  $\sim 18$  Ma, the triple junction of the Nazca, Phoenix, and Antarctic plates began to subduct, and after  $\sim 10$  Ma, the Nazca–Phoenix Ridge completely subducted, leaving only a triple junction between Nazca, Antarctica, and South America (Breitsprecher & Thorkelson, 2009). This tectonic history suggests that spreading ridge subduction in the F1 region extended back to at least  $\sim 50$  Ma (Gianni et al., 2018).

Assuming that the anomaly amplitude is sufficiently recovered based on the results of the synthetic recovery test, the maximum amplitude of the anomaly is  $\sim 1.0\%$  for F1 and  $\sim 2.0\%$  for the subducted Nazca slab at F1 depth. The seismic velocity anomaly was related to the temperature anomaly using the following equation (Karato, 1993):

$$\partial T = \left( \frac{\partial \ln v_0}{\partial T} - \frac{H^*}{Q\pi R} \frac{1}{T^2} \right)^{-1} \frac{\partial v}{v} \quad (6)$$

where  $T$  is temperature,  $v$  is seismic velocity,  $H^*$  is activation enthalpy,  $Q$  is a seismic quality factor and  $R$  is gas constant. In the upper part of the transition zone, a difference in velocity anomaly of 1% between the F1 and the Nazca slab corresponds to a temperature difference of approximately 210 K with  $\partial \ln v_0 / \partial T = 5.27 \times 10^5$  1/K (Karato, 1993),  $T = 1,938$  K (Katsura, 2022),  $T = 1,938$  K,  $Q = 143$  (PREM: Dziewonski & Anderson, 1981),  $H^* = 80$  kJ/mol (Dai & Karato, 2009) and  $R = 8.13$  J/(K · mol). From numerical simulations, it takes  $\sim 30$  Myr for the stagnant slab to warm to 200 K in the transition zone, although this time highly depends on the properties of the slab and the surrounding mantle (e.g., Motoki & Ballmer, 2015). Therefore, if F1 was a detached Phoenix plate, the amplitude of its fast anomaly should be much smaller after remaining stagnant in the transition zone for approximately 50 Myr.

Although we focused on the F1 anomaly in this paper, the resulting model also resolved the geometry of the Nazca slab clearly, offering insights into its evolutionary patterns. As seen in synthetic recovery tests, the Nazca slab anomaly had a reduced amplitude toward the south due to limited ray sampling. Such changes in resolution with location should be considered; however, we may be able to speculate the noted variations in slab geometry as the proxy for variation of sunken slabs over time. The strike and subduction rates along the Chile Trench south of  $20^\circ$  are relatively constant while the age of the oceanic plate becomes younger to the south. Therefore, in a simplified view, the southern cross section represents the slab's condition after a longer period since its subduction. Figures 6d and 6e show that the F1 anomaly was interrupted in the upper mantle as if the slab had detached. Moreover, the lower part of the slab continued deeper to the south, giving the idea that the slab had detached and then was gradually sinking. In contrast, on the east side of the upper slab there were horizontally lying high velocity anomalies. These were not continuous to the surface and therefore they were unlikely to be high velocity anomalies associated with the influence of cratons observed in the northern region (Rocha et al., 2011). Although it was difficult to completely separate the horizontal smearing from the slab anomaly in our final model, these structures, together with future numerical calculations and geophysical observations, will contribute to understanding of the development of the Nazca slab subduction.

### 5.3. Patagonian Slab Window

Our model showed a prominent low-velocity anomaly (S1) in the putative extension of the Patagonian slab window on the eastern side of the CTJ (Figures 5 and 11). The strongest anomaly was  $\sim 1.6\%$  at a latitude of  $\sim 48^\circ\text{S}$  and a depth of  $\sim 130$  km. The center of S1 coincided with the approximate location of the spreading ridge segment between the Tres Montes and Esmeralda fracture zones (green dotted line in Figure 5). The northern and western edges of S1 are bounded by the extension of the Taitao transform fault and CTJ, respectively, which constrain the edge of the Patagonian slab window. The eastern end was not well-constrained by our model because of its low resolution, as indicated by the synthetic recovery test. Further measurements extending east of our study region would help illuminate the eastern edge of the Patagonian slab window. North of  $\sim 50^\circ\text{S}$ , the western edge of S1 is consistent with prior imaging and the inferred extension (Breitsprecher & Thorkelson, 2009; Mark et al., 2022; Russo et al., 2010). South of  $\sim 50^\circ\text{S}$ , the southern edge of the low-velocity anomaly is farther north than that predicted by the kinematic reconstruction at depths shallower than 100 km, but generally agrees with the prediction at depths deeper than 100 km. Considering the results of the synthetic recovery tests, the

resulting velocity model indicates that the low-velocity anomalies associated with the slab window are continuous up to a depth of at least 200 km and do not extend to depths greater than 300 km.

At the surface, the active adakitic volcanoes in southern Patagonia are considered a result from the partial melting of the trailing young plate edges along a slab window margin that borders the southern edge of S1. The S1 area also agrees with the proposed volcanic gap, which suggests that there is no dehydration from the slab and that the upper mantle in this region may be highly depleted and have a low water content (Ben-Mansour et al., 2022; Ramos & Kay, 1992). In the back-arc region, S1 covered the distribution of plateau lavas younger than 3.3 Myr. These plateau lavas originate from decompression melting of the subslab asthenosphere through the slab window (Gorring & Kay, 2001).

The anomalously slow seismic velocities observed within the Patagonian slab window have been attributed to high temperatures caused by mantle upwelling, which compensates for the window and thermal erosion of the lithospheric mantle (Mark et al., 2022). Mantle upwelling in the area of the window is supported by studies on extensive Neogene Patagonian plateau lavas (e.g., Gorring et al., 1997), and net upflow can occur through the window depending on differential density, rheology, or pressure (Thorkelson, 1996). The slow anomalies throughout S1 indicate that the slab window was filled with hot material from the deeper mantle at depths of up to 250 km. The estimated depth range of the slab window also agrees with the vertical extent of the slab gap, to which upwelling can occur in the laboratory model (Király et al., 2020). In contrast, Sanhueza et al. (2023) recently conducted a numerical modeling study on the geodynamic processes caused by ridge subduction at the CTJ and suggested that asthenospheric upflow could only occur for a short time (~2 Myr) associated with the beginning of window opening. Instead, they proposed that horizontal flow from the oceanic mantle to the continental mantle might be more efficient for temperature changes. In addition, shear wave splitting analyses showed a strong EW fast direction in the vicinity of the CTJ, indicating vigorous mantle flow through the window (Ben-Mansour et al., 2022; Russo et al., 2010). Since the Chile Ridge began to subduct at around 54°S at 18 Ma, the CTJ has been migrating northward over time. Therefore, the north-south change in the cross sections can be interpreted as a proxy for the time lapse since the ridge axis was subducted. Figures 6g–6i showed that the amplitude of S1 becomes smaller to the south and gradually shifts to the east. This structure may imply that the slow anomalies are like high-temperature anomalies that were generated just after the ridge subduction and are gradually weakening, rather than like a plume from the deep mantle. It is also inferred that the mantle flow is not highly turbulent, and these interpretations are consistent with Sanhueza et al. (2023).

## 6. Conclusions

We performed hybrid finite-frequency and ray-theoretical tomography to obtain a new P-wave velocity model for Southern South America. Approximately 1,600 arrivals and 224 thousand differential traveltimes were picked from broadband seismic stations, including our temporal OBS arrays at the CTJ, and 31 million global traveltimes data from the ISC were used for inversion. The resulting tomography image showed some notable features of the mantle structure up to the uppermost part of the lower mantle at a depth of ~1,000 km (Figure 11).

- (1) A fast anomaly extending beneath the Nazca slab was approximately parallel to the Nazca slab between 26° and 35°S. This fast anomaly beneath the Nazca slab may be a relic of the Nazca slab associated with flat slab subduction, based on its location, geometry, and anomaly amplitude.
- (2) A strong, slow anomaly on the east of the CTJ, which is consistent with the extent of the Patagonian slab window. Our model indicated that slow anomalies associated with the slab window persisted up to depths of approximately 250 km.

## Data Availability Statement

OBS data in the vicinity of the Chile Triple Junction are available from the Ocean Hemisphere Project Data Management Center, Earthquake Research Institute, University of Tokyo (OHPDMC, 2024). All seismograms from onshore stations are available from the Incorporated Research Institutions for Seismology Data Management Center the EarthScope Consortium Web Services (<https://service.iris.edu/>). These include the following seismic networks with Federation of Digital Seismograph Networks (FDSN) codes 1P (Wiens & Magnani, 2018), AI (OGS, 1992), C (National Seismological Center, 1991), C1 (Universidad de Chile, 2012), G (IPGP & EOST, 1982), GT (ASL-USGS, 1993), II (SIO, 1986), IU (ASL-USGS, 2014), ON (ON, 2011), and YT (Wiens

et al., 2007). Global onset time data used in this study are publicly available through (ISC, 2022). Some figures were generated with the Generic Mapping Tools (Wessel et al., 2019) and the ParaView (Ahrens et al., 2005; Ayachit, 2015).

## Acknowledgments

In this study, we used the computer systems of the Earthquake and Volcano Information Center of the Earthquake Research Institute of the University of Tokyo. We thank the IRIS Data Management Center for providing the seismograms used in this study. Genetic Mapping Tools 6.4.0 (<https://www.generic-mapping-tools.org/download/>), developed by Wessel et al. (2019), was used to create the figures. This work was supported by JSPS KAKENHI Grant 23KJ1568 for YK and 18H01304 for MK. JO acknowledges support from the Agencia Nacional de Investigación y Desarrollo (Scholarship ANID-PCFCHA/Doctorado Nacional/2020-21200903). We would like to thank Associate Editor Fenglin Niu and the anonymous reviewers for their careful and constructive reviews, which have significantly improved our manuscript.

## References

- Agurto-Detzel, H., Rietbrock, A., Bataille, K., Miller, M., Iwamori, H., & Priestley, K. (2014). Seismicity distribution in the vicinity of the Chile Triple Junction, Aysén Region, southern Chile. *Journal of South American Earth Sciences*, 51, 1–11. <https://doi.org/10.1016/j.jsames.2013.12.011>
- Ahrens, J., Geveci, B., & Law, C. (2005). ParaView: An end-user tool for large data visualization [Software]. In *Visualization handbook*. Elsevier. <https://doi.org/10.1016/B978-012387582-2/50038-1>
- Amaru, M. (2007). Global travel time tomography with 3-D reference models.
- Antonijevic, S., Wagner, L. S., Beck, S. L., Long, M. D., Zandt, G., & Tavera, H. (2016). Effects of change in slab geometry on the mantle flow and slab fabric in southern Peru. *Journal of Geophysical Research: Solid Earth*, 121(10), 7252–7270. <https://doi.org/10.1002/2016JB013064>
- Arrial, P.-A., & Billen, M. I. (2013). Influence of geometry and eclogitization on oceanic plateau subduction. *Earth and Planetary Science Letters*, 363, 34–43. <https://doi.org/10.1016/j.epsl.2012.12.011>
- ASL-USGS (1993). Albuquerque seismic laboratory (ASL)/USGS, global telemetered seismograph network (USA/USGS). *International Federation of Digital Seismograph Networks*. <https://doi.org/10.7914/SN/GT>
- ASL-USGS. (2014). Albuquerque seismic laboratory/USGS, global seismograph network (GSN—IRIS/USGS) [Dataset]. *International Federation of Digital Seismograph Networks*. <https://doi.org/10.7914/SN/IU>
- Ávila, P., & Dávila, F. M. (2018). Heat flow and lithospheric thickness analysis in the Patagonian asthenospheric windows, southern South America. *Tectonophysics*, 747–748, 99–107. <https://doi.org/10.1016/j.tecto.2018.10.006>
- Axen, G. J., van Wijk, J. W., & Currie, C. A. (2018). Basal continental mantle lithosphere displaced by flat-slab subduction. *Nature Geoscience*, 11(12), 961–964. <https://doi.org/10.1038/s41561-018-0263-9>
- Ayachit, U. (2015). *The ParaView guide: A parallel visualization application* [Software]. Kitware. Retrieved from <https://dl.acm.org/doi/10.5555/2789330>
- Bangs, N. L., & Cande, S. C. (1997). Episodic development of a convergent margin inferred from structures and processes along the southern Chile margin. *Tectonics*, 16(3), 489–503. <https://doi.org/10.1029/97TC00494>
- Barazangi, M., & Isacks, B. L. (1976). Spatial distribution of earthquakes and subduction of the Nazca plate beneath South America. *Geology*, 4(11), 686–692. [https://doi.org/10.1130/0091-7613\(1976\)4<686:SDOEAS>2.0.CO;2](https://doi.org/10.1130/0091-7613(1976)4<686:SDOEAS>2.0.CO;2)
- Bassin, C., Laskie, G., & Masters, G. (2000). The current limits of resolution for surface wave tomography in North America. *Eos, Transactions American Geophysical Union*, 81(F897).
- Ben-Mansour, W., Wiens, D. A., Mark, H. F., Russo, R. M., Richter, A., Marderwald, E., & Barrientos, S. (2022). Mantle flow pattern associated with the Patagonian slab window determined from azimuthal anisotropy. *Geophysical Research Letters*, 49(18), e2022GL099871. <https://doi.org/10.1029/2022GL099871>
- Bianchi, M., Heit, B., Jakovlev, A., Yuan, X., Kay, S. M., Sandvol, E., et al. (2013). Teleseismic tomography of the southern Puna plateau in Argentina and adjacent regions. *Tectonophysics*, 586, 65–83. <https://doi.org/10.1016/j.tecto.2012.11.016>
- Bourgois, J., Guivel, C., Lagabrielle, Y., Calmus, T., Boulègue, J., & Daux, V. (2000). Glacial-interglacial trench supply variation, spreading-ridge subduction, and feedback controls on the Andean margin development at the Chile triple junction area (45–48°S). *Journal of Geophysical Research*, 105(B4), 8355–8386. <https://doi.org/10.1029/1999JB900400>
- Bourgois, J., Lagabrielle, Y., Martin, H., Dymnt, J., Frutos, J., & Cisternas, M. E. (2016). A review on forearc ophiolite obduction, adakite-like generation, and slab window development at the Chile triple junction area: Uniformitarian framework for spreading-ridge subduction. *Pure and Applied Geophysics*, 173(10), 3217–3246. <https://doi.org/10.1007/s0024-016-1317-9>
- Bourgois, J., Martin, H., Lagabrielle, Y., Le Moigne, J., & Frutos Jara, J. (1996). Subduction erosion related to spreading-ridge subduction: Taitao peninsula (Chile margin triple junction area). *Geology*, 24(8), 723. [https://doi.org/10.1130/0091-7613\(1996\)024<0723:SERTSR>2.3.CO;2](https://doi.org/10.1130/0091-7613(1996)024<0723:SERTSR>2.3.CO;2)
- Boutonnet, E., Arnaud, N., Guivel, C., Lagabrielle, Y., Scalabrinio, B., & Espinoza, F. (2010). Subduction of the South Chile active spreading ridge: A 17Ma to 3Ma magmatic record in central Patagonia (western edge of Meseta del Lago Buenos Aires, Argentina). *Journal of Volcanology and Geothermal Research*, 189(3), 319–339. <https://doi.org/10.1016/j.jvolgeores.2009.11.022>
- Breitsprecher, K., & Thorkelson, D. J. (2009). Neogene kinematic history of Nazca–Antarctic–Phoenix slab windows beneath Patagonia and the Antarctic Peninsula. *Tectonophysics*, 464(1–4), 10–20. <https://doi.org/10.1016/j.tecto.2008.02.013>
- Burd, A. I., Booker, J. R., Mackie, R., Pomposiello, C., & Favetto, A. (2013). Electrical conductivity of the Pampean shallow subduction region of Argentina near 33°S: Evidence for a slab window. *Geochemistry, Geophysics, Geosystems*, 14(8), 3192–3209. <https://doi.org/10.1002/ggge.20213>
- Cahill, T., & Isacks, B. L. (1992). Seismicity and shape of the subducted Nazca Plate. *Journal of Geophysical Research*, 97(B12), 17503–17529. <https://doi.org/10.1029/92JB00493>
- Cande, S. C., & Leslie, R. B. (1986). Late Cenozoic tectonics of the southern Chile Trench. *Journal of Geophysical Research*, 91(B1), 471–496. <https://doi.org/10.1029/JB091iB01p00471>
- Cande, S. C., Leslie, R. B., Parra, J. C., & Hobart, M. (1987). Interaction between the Chile Ridge and Chile Trench: Geophysical and geothermal evidence. *Journal of Geophysical Research*, 92(B1), 495–520. <https://doi.org/10.1029/JB092iB01p00495>
- Celli, N. L., Lebedev, S., Schaeffer, A. J., Ravenna, M., & Gaiña, C. (2020). The upper mantle beneath the South Atlantic Ocean, South America and Africa from waveform tomography with massive data sets. *Geophysical Journal International*, 221(1), 178–204. <https://doi.org/10.1093/gji/ggz574>
- Chen, Y.-W., Wu, J., & Suppe, J. (2019). Southward propagation of Nazca subduction along the Andes. *Nature*, 565(7740), 441–447. <https://doi.org/10.1038/s41586-018-0860-1>
- Ciardelli, C., Assumpção, M., Bozdağ, E., & van der Lee, S. (2022). Adjoint waveform tomography of South America. *Journal of Geophysical Research: Solid Earth*, 127(2), e2021JB022575. <https://doi.org/10.1029/2021JB022575>
- Cristallini, E. O., & Ramos, V. A. (2000). Thick-skinned and thin-skinned thrusting in the La Ramada fold and thrust belt: Crustal evolution of the High Andes of San Juan, Argentina (32°SL). *Tectonophysics*, 317(3–4), 205–235. [https://doi.org/10.1016/S0040-1951\(99\)00276-0](https://doi.org/10.1016/S0040-1951(99)00276-0)
- Dahlen, F. A., Hung, S.-H., & Nolet, G. (2000). Fréchet kernels for finite-frequency traveltimes-I. Theory. *Geophysical Journal International*, 141(1), 157–174. <https://doi.org/10.1046/j.1365-246X.2000.00070.x>

- Dai, L., & Karato, S. (2009). Electrical conductivity of wadsleyite at high temperatures and high pressures. *Earth and Planetary Science Letters*, 287(1–2), 277–283. <https://doi.org/10.1016/j.epsl.2009.08.012>
- Dai, L., Wang, L., Lou, D., Li, Z.-H., Dong, H., Ma, F., et al. (2020). Slab rollback versus delamination: Contrasting fates of flat-slab subduction and implications for South China evolution in the Mesozoic. *Journal of Geophysical Research: Solid Earth*, 125(4), e2019JB019164. <https://doi.org/10.1029/2019JB019164>
- Dávila, F. M., & Lithgow-Bertelloni, C. (2013). Dynamic topography in South America. *Journal of South American Earth Sciences*, 43, 127–144. <https://doi.org/10.1016/j.jsames.2012.12.002>
- DeLong, S. E., Schwarz, W. M., & Anderson, R. N. (1979). Thermal effects of ridge subduction. *Earth and Planetary Science Letters*, 44(2), 239–246. [https://doi.org/10.1016/0012-821X\(79\)90172-9](https://doi.org/10.1016/0012-821X(79)90172-9)
- DeMets, C., Gordon, R. G., & Argus, D. F. (2010). Geologically current plate motions. *Geophysical Journal International*, 181(1), 1–80. <https://doi.org/10.1111/j.1365-246X.2009.04491.x>
- Dickinson, W. R., & Snyder, W. S. (1979). Geometry of subducted slabs related to San Andreas transform. *The Journal of Geology*, 87(6), 609–627. <https://doi.org/10.1086/628456>
- Dziewonski, A., & Gilbert, F. (1976). The effect of small, aspherical perturbations on travel times and a re-examination of the corrections for ellipticity. *Geophysical Journal of the Royal Astronomical Society*, 44(1), 7–17. <https://doi.org/10.1111/j.1365-246X.1976.tb00271.x>
- Dziewonski, A. M., & Anderson, D. L. (1981). Preliminary reference Earth model. *Physics of the Earth and Planetary Interiors*, 25(4), 297–356. [https://doi.org/10.1016/0031-9201\(81\)90046-7](https://doi.org/10.1016/0031-9201(81)90046-7)
- Eagles, G., Gohl, K., & Larter, R. D. (2009). Animated tectonic reconstruction of the southern Pacific and alkaline volcanism at its convergent margins since Eocene times. *Tectonophysics*, 464(1–4), 21–29. <https://doi.org/10.1016/j.tecto.2007.10.005>
- Espinosa, F., Morata, D., Pelletier, E., Maury, R. C., Suárez, M., Lagabrielle, Y., et al. (2005). Petrogenesis of the Eocene and Mio-Pliocene alkaline basaltic magmatism in Meseta Chile Chico, southern Patagonia, Chile: Evidence for the participation of two slab windows. *Lithos*, 82(3), 315–343. <https://doi.org/10.1016/j.lithos.2004.09.024>
- Esprut, N., Funiciello, F., Martinod, J., Guillaume, B., Regard, V., Faccenna, C., & Brusset, S. (2008). Flat subduction dynamics and deformation of the South American plate: Insights from analog modeling. *Tectonics*, 27(3). <https://doi.org/10.1029/2007TC002175>
- Feng, M., van der Lee, S., & Assumpção, M. (2007). Upper mantle structure of South America from joint inversion of waveforms and fundamental mode group velocities of Rayleigh waves. *Journal of Geophysical Research*, 112(B4), B04312. <https://doi.org/10.1029/2006JB004449>
- Forsythe, R. D., Nelson, E. P., Carr, M. J., Kaeding, M. E., Herve, M., Mpodozis, C., et al. (1986). Pliocene near-trench magmatism in southern Chile: A possible manifestation of ridge collision. *Geology*, 14(1), 23–27. [https://doi.org/10.1130/0091-7613\(1986\)14<23:PNMISC>2.0.CO;2](https://doi.org/10.1130/0091-7613(1986)14<23:PNMISC>2.0.CO;2)
- Gallego, A., Russo, R. M., Comte, D., Mocanu, V. I., Murdie, R. E., & Vandecar, J. C. (2010). Seismic noise tomography in the Chile ridge subduction region: Seismic noise recorded in the CTJ. *Geophysical Journal International*, 182(3), 1478–1492. <https://doi.org/10.1111/j.1365-246X.2010.04691.x>
- Gao, Y., Yuan, X., Heit, B., Tilmann, F., van Herwaarden, D.-P., Thrastarson, S., et al. (2021). Impact of the Juan Fernandez Ridge on the Pampean flat subduction inferred from full waveform inversion. *Geophysical Research Letters*, 48(21), e2021GL095509. <https://doi.org/10.1029/2021GL095509>
- Gianni, G. M., Pesce, A., & Soler, S. R. (2018). Transient plate contraction between two simultaneous slab windows: Insights from Paleogene tectonics of the Patagonian Andes. *Journal of Geodynamics*, 121, 64–75. <https://doi.org/10.1016/j.jog.2018.07.008>
- Goldstein, P., Dodge, D., Firpo, M., & Minner, L. (2003). SAC2000: Signal processing and analysis tools for seismologists and engineers. In *International geophysics* (pp. 1613–1614). Elsevier. [https://doi.org/10.1016/S0074-6142\(03\)80284-X](https://doi.org/10.1016/S0074-6142(03)80284-X)
- Gorring, M. L., & Kay, S. M. (2001). Mantle processes and sources of Neogene slab window magmas from southern Patagonia, Argentina. *Journal of Petrology*, 42(6), 1067–1094. <https://doi.org/10.1093/petrology/42.6.1067>
- Gorring, M. L., Kay, S. M., Zeitler, P. K., Ramos, V. A., Rubiolo, D., Fernandez, M. I., & Panza, J. L. (1997). Neogene Patagonian plateau lavas: Continental magmas associated with ridge collision at the Chile triple junction. *Tectonics*, 16(1), 1–17. <https://doi.org/10.1029/96TC03368>
- Groome, W. G., & Thorkelson, D. J. (2009). The three-dimensional thermo-mechanical signature of ridge subduction and slab window migration. *Tectonophysics*, 464(1–4), 70–83. <https://doi.org/10.1016/j.tecto.2008.07.003>
- Guillaume, B., Martinod, J., Husson, L., Roddaz, M., & Riquelme, R. (2009). Neogene uplift of central eastern Patagonia: Dynamic response to active spreading ridge subduction. *Tectonics*, 28(2), TC2009. <https://doi.org/10.1029/2008TC002324>
- Guillaume, B., Moroni, M., Funiciello, F., Martinod, J., & Faccenna, C. (2010). Mantle flow and dynamic topography associated with slab window opening: Insights from laboratory models. *Tectonophysics*, 496(1), 83–98. <https://doi.org/10.1016/j.tecto.2010.10.014>
- Gutiérrez, F., Giocnada, A., González Ferran, O., Lahsen, A., & Mazzuoli, R. (2005). The Hudson Volcano and surrounding monogenetic centres (Chilean Patagonia): An example of volcanism associated with ridge-trench collision environment. *Journal of Volcanology and Geothermal Research*, 145(3–4), 207–233. <https://doi.org/10.1016/j.jvolgeores.2005.01.014>
- Gutscher, M.-A. (2002). Andean subduction styles and their effect on thermal structure and interplate coupling. *Journal of South American Earth Sciences*, 15(1), 3–10. [https://doi.org/10.1016/S0895-9811\(02\)00002-0](https://doi.org/10.1016/S0895-9811(02)00002-0)
- Gutscher, M.-A., Spakman, W., Bijwaard, H., & Engdahl, E. R. (2000). Geodynamics of flat subduction: Seismicity and tomographic constraints from the Andean margin. *Tectonics*, 19(5), 814–833. <https://doi.org/10.1029/1999TC001152>
- Hayes, G. P., Moore, G. L., Portner, D. E., Hearne, M., Flammé, H., Furtney, M., & Smoczyk, G. M. (2018). Slab2, a comprehensive subduction zone geometry model. *Science*, 362(6410), 58–61. <https://doi.org/10.1126/science.aat4723>
- Horton, B. K. (2018). Tectonic regimes of the central and southern Andes: Responses to variations in plate coupling during subduction. *Tectonics*, 37(2), 402–429. <https://doi.org/10.1029/2017TC004624>
- Hung, S.-H., Dahlen, F. A., & Nolet, G. (2000). Fréchet kernels for finite-frequency traveltimes-II. Examples. *Geophysical Journal International*, 141(1), 175–203. <https://doi.org/10.1046/j.1365-246X.2000.00072.x>
- Inoue, H., Fukao, Y., Tanabe, K., & Ogata, Y. (1990). Whole mantle P-wave travel time tomography. *Physics of the Earth and Planetary Interiors*, 59(4), 294–328. [https://doi.org/10.1016/0031-9201\(90\)90236-Q](https://doi.org/10.1016/0031-9201(90)90236-Q)
- IPGP & EOST. (1982). Institut de physique du globe de Paris, & École et Observatoire des Sciences de la Terre de Strasbourg, GEOSCOPE, French Global Network of broad band seismic stations [Dataset]. *Institut de physique du globe de Paris (IPGP), Université de Paris*. <https://doi.org/10.18715/GEOSCOPE.G>
- ISC. (2022). International seismological centre [Dataset]. *On-line Bulletin*. <https://doi.org/10.31905/D808B830>
- Ito, A., Shiobara, H., Miller, M., Sugioka, H., Ojeda, J., Tassara, C., et al. (2023). Long-term array observation by ocean bottom seismometers at the Chile triple junction. *Journal of South American Earth Sciences*, 124, 104285. <https://doi.org/10.1016/j.jsames.2023.104285>
- Kaeding, M., Forsythe, R. D., & Nelson, E. P. (1990). Geochemistry of the Taïtao ophiolite and near-trench intrusions from the Chile margin triple junction. *Journal of South American Earth Sciences*, 3(4), 161–177. [https://doi.org/10.1016/0895-9811\(90\)90001-H](https://doi.org/10.1016/0895-9811(90)90001-H)

- Karato, S. (1993). Importance of anelasticity in the interpretation of seismic tomography. *Geophysical Research Letters*, 20(15), 1623–1626. <https://doi.org/10.1029/93GL01767>
- Karsten, J. L., Klein, E. M., & Sherman, S. B. (1996). Subduction zone geochemical characteristics in ocean ridge basalts from the southern Chile Ridge: Implications of modern ridge subduction systems for the Archean. *Lithos*, 37(2–3), 143–161. [https://doi.org/10.1016/0024-4937\(95\)00034-8](https://doi.org/10.1016/0024-4937(95)00034-8)
- Katsura, T. (2022). A revised adiabatic temperature profile for the mantle. *Journal of Geophysical Research: Solid Earth*, 127(2), e2021JB023562. <https://doi.org/10.1029/2021JB023562>
- Kay, S. M., & Coira, B. L. (2009). Shallowing and steepening subduction zones, continental lithospheric loss, magmatism, and crustal flow under the Central Andean Altiplano-Puna Plateau. In S. M. Kay, V. A. Ramos, & W. R. Dickinson (Eds.), *Backbone of the Americas: Shallow subduction, Plateau uplift, and ridge and terrane collision*. Geological Society of America. [https://doi.org/10.1130/2009.1204\(11\)](https://doi.org/10.1130/2009.1204(11))
- Kay, S. M., & Mpodozis, C. (2002). Magmatism as a probe to the Neogene shallowing of the Nazca plate beneath the modern Chilean flat-slab. *Journal of South American Earth Sciences*, 15(1), 39–57. [https://doi.org/10.1016/S0895-9811\(02\)00005-6](https://doi.org/10.1016/S0895-9811(02)00005-6)
- Kennett, B. L. N., & Engdahl, E. R. (1991). Traveltimes for global earthquake location and phase identification. *Geophysical Journal International*, 105(2), 429–465. <https://doi.org/10.1111/j.1365-246X.1991.tb06724.x>
- Király, Á., Portner, D. E., Haynie, K. L., Chilson-Parks, B. H., Ghosh, T., Jadamec, M., et al. (2020). The effect of slab gaps on subduction dynamics and mantle upwelling. *Tectonophysics*, 785, 228458. <https://doi.org/10.1016/j.tecto.2020.228458>
- Lagabrielle, Y., Guivel, C., Maury, R. C., Bourgois, J., Fourcade, S., & Martin, H. (2000). Magmatic–tectonic effects of high thermal regime at the site of active ridge subduction: The Chile triple junction model. *Tectonophysics*, 326(3–4), 255–268. [https://doi.org/10.1016/S0040-1951\(00\)00124-4](https://doi.org/10.1016/S0040-1951(00)00124-4)
- Lagabrielle, Y., Moigne, J. L., Maury, R. C., Cotten, J., & Bourgois, J. (1994). Volcanic record of the subduction of an active spreading ridge, Taitao Peninsula (southern Chile). *Geology*, 22(6), 515–518. [https://doi.org/10.1130/0091-7613\(1994\)022<0515:VROS>2.3.CO;2](https://doi.org/10.1130/0091-7613(1994)022<0515:VROS>2.3.CO;2)
- Li, C., van der Hilst, R. D., Engdahl, E. R., & Burdick, S. (2008). A new global model for P wave speed variations in Earth's mantle. *Geochemistry, Geophysics, Geosystems*, 9(5), Q05018. <https://doi.org/10.1029/2007GC001806>
- Liu, S., & Currie, C. A. (2016). Farallon plate dynamics prior to the Laramide orogeny: Numerical models of flat subduction. *Tectonophysics*, 666, 33–47. <https://doi.org/10.1016/j.tecto.2015.10.010>
- Liu, X., & Currie, C. A. (2019). Influence of upper plate structure on flat-slab depth: Numerical modeling of subduction dynamics. *Journal of Geophysical Research: Solid Earth*, 124(12), 13150–13167. <https://doi.org/10.1029/2019JB018653>
- Lu, C., Grand, S. P., Lai, H., & Garnero, E. J. (2019). TX2019slab: A new P and S tomography model incorporating subducting slabs. *Journal of Geophysical Research: Solid Earth*, 124(11), 11549–11567. <https://doi.org/10.1029/2019JB017448>
- Lynner, C., Anderson, M. L., Portner, D. E., Beck, S. L., & Gilbert, H. (2017). Mantle flow through a tear in the Nazca slab inferred from shear wave splitting. *Geophysical Research Letters*, 44(13), 6735–6742. <https://doi.org/10.1002/2017GL074312>
- Ma, Y., & Clayton, R. W. (2014). The crust and uppermost mantle structure of southern Peru from ambient noise and earthquake surface wave analysis. *Earth and Planetary Science Letters*, 395, 61–70. <https://doi.org/10.1016/j.epsl.2014.03.013>
- Maksymowicz, A., Contreras-Reyes, E., Grevemeyer, I., & Flueh, E. R. (2012). Structure and geodynamics of the post-collision zone between the Nazca–Antarctic spreading center and South America. *Earth and Planetary Science Letters*, 345, 27–37. <https://doi.org/10.1016/j.epsl.2012.06.023>
- Manea, V. C., Manea, M., Ferrari, L., Orozco-Esquivel, T., Valenzuela, R. W., Husker, A., & Kostoglodov, V. (2017). A review of the geo-dynamic evolution of flat slab subduction in Mexico, Peru, and Chile. *Tectonophysics*, 695, 27–52. <https://doi.org/10.1016/j.tecto.2016.11.037>
- Manea, V. C., Pérez-Gussinyé, M., & Manea, M. (2012). Chilean flat slab subduction controlled by overriding plate thickness and trench rollback. *Geology*, 40(1), 35–38. <https://doi.org/10.1130/G32543.1>
- Mark, H. F., Wiens, D. A., Ivins, E. R., Richter, A., Ben Mansour, W., Magnani, M. B., et al. (2022). Lithospheric erosion in the Patagonian slab window, and implications for glacial isostasy. *Geophysical Research Letters*, 49(2), e2021GL096863. <https://doi.org/10.1029/2021GL096863>
- Marot, M., Monfret, T., Gerbault, M., Nolet, G., Ranalli, G., & Pardo, M. (2014). Flat versus normal subduction zones: A comparison based on 3-D regional traveltimes tomography and petrological modelling of central Chile and western Argentina (29°–35°S). *Geophysical Journal International*, 199(3), 1633–1654. <https://doi.org/10.1093/gji/ggu355>
- Martinod, J., Guillaume, B., Espurt, N., Faccenna, C., Funiciello, F., & Regard, V. (2013). Effect of aseismic ridge subduction on slab geometry and overriding plate deformation: Insights from analogue modeling. *Tectonophysics*, 588, 39–55. <https://doi.org/10.1016/j.tecto.2012.12.010>
- Miller, M., Priestley, K., Tilmann, F., Bataille, K., & Iwamori, H. (2023). P wave teleseismic tomography of the subducted Chile rise. *Journal of South American Earth Sciences*, 128, 104447. <https://doi.org/10.1016/j.jsames.2023.104474>
- Mohammadzaheri, A., Sigloch, K., Hosseini, K., & Mihalynuk, M. G. (2021). Subducted lithosphere under South America from multifrequency P wave tomography. *Journal of Geophysical Research: Solid Earth*, 126(6), e2020JB020704. <https://doi.org/10.1029/2020JB020704>
- Montelli, R., Nolet, G., Masters, G., Dahlen, F. A., & Hung, S.-H. (2004). Global P and PP traveltimes tomography: Rays versus waves. *Geophysical Journal International*, 158(2), 637–654. <https://doi.org/10.1111/j.1365-246X.2004.02346.x>
- Motoki, M. H., & Ballmer, M. D. (2015). Intraplate volcanism due to convective instability of stagnant slabs in the mantle transition zone. *Geochemistry, Geophysics, Geosystems*, 16(2), 538–551. <https://doi.org/10.1002/2014GC005608>
- Müller, R. D., Sdrolias, M., Gaina, C., & Roest, W. R. (2008). Age, spreading rates, and spreading asymmetry of the world's ocean crust. *Geochemistry, Geophysics, Geosystems*, 9(4), Q04006. <https://doi.org/10.1029/2007GC001743>
- Murdie, R. E., Styles, P., Prior, D. J., & Daniel, A. J. (2000). A new gravity map of southern Chile and its preliminary interpretation. *Revista Geológica de Chile*, 27(1), 49–63. <https://doi.org/10.4067/S0716-02082000000100004>
- National Seismological Center. (1991). Chilean National Seismic Network [Dataset]. Retrieved from <https://www.plataformadedatos.cl/datasets/en/80ABA1DC1DD80F2C>
- Nelson, E., Forsythe, R., Diemer, J., Allen, M., & Urbina, O. (1993). Taitao ophiolite: A ridge collision ophiolite in the forearc of southern Chile (460°S). *Revista Geológica de Chile*, 20(2), 137–165.
- Obayashi, M., Ishihara, Y., & Suetsugu, D. (2017). Effects of shallow-layer reverberation on measurement of teleseismic P-wave travel times for ocean bottom seismograph data. *Earth Planets and Space*, 69(1), 44. <https://doi.org/10.1186/s40623-017-0626-2>
- Obayashi, M., Yoshimitsu, J., Nolet, G., Fukao, Y., Shiobara, H., Sugioka, H., et al. (2013). Finite frequency whole mantle P wave tomography: Improvement of subducted slab images. *Geophysical Research Letters*, 40(21), 5652–5657. <https://doi.org/10.1002/2013GL057401>
- OGS. (1992). Istituto Nazionale di Oceanografia e di Geofisica Sperimentale, Antarctic Seismographic Argentinean Italian Network—ASAIN [Dataset]. *International Federation of Digital Seismograph Networks*. <https://doi.org/10.7914/SN/AI>
- OHP DMC. (2024). Ocean hemisphere project data management center [Dataset]. Retrieved from <http://ohp-dc.eri.u-tokyo.ac.jp:8080/fdsnws/datasetselect/>

- ON. (2011). Observatório Nacional, Rio de Janeiro, RJ, Rede Sismográfica do Sul e do Sudeste [Dataset]. *International Federation of Digital Seismograph Networks*. <https://doi.org/10.7914/SN/ON>
- Pardo, M., Comte, D., & Monfret, T. (2002). Seismotectonic and stress distribution in the central Chile subduction zone. *Journal of South American Earth Sciences*, 15(1), 11–22. [https://doi.org/10.1016/S0895-9811\(02\)00003-2](https://doi.org/10.1016/S0895-9811(02)00003-2)
- Pesicek, J. D., Engdahl, E. R., Thurber, C. H., DeShon, H. R., & Lange, D. (2012). Mantle subducting slab structure in the region of the 2010 M8.8 Maule earthquake (30–40°S), Chile: Mantle subducting slab structure in Chile. *Geophysical Journal International*, 191(1), 317–324. <https://doi.org/10.1111/j.1365-246X.2012.05624.x>
- Porter, R., Gilbert, H., Zandt, G., Beck, S., Warren, L., Calkins, J., et al. (2012). Shear wave velocities in the Pampean flat-slab region from Rayleigh wave tomography: Implications for slab and upper mantle hydration. *Journal of Geophysical Research*, 117(B11), B11301. <https://doi.org/10.1029/2012JB009350>
- Portner, D. E., Beck, S., Zandt, G., & Scire, A. (2017). The nature of subslab slow velocity anomalies beneath South America. *Geophysical Research Letters*, 44(10), 4747–4755. <https://doi.org/10.1002/2017GL073106>
- Portner, D. E., Rodríguez, E. E., Beck, S., Zandt, G., Scire, A., Rocha, M. P., et al. (2020). Detailed structure of the subducted Nazca slab into the lower mantle derived from continent-scale teleseismic P wave tomography. *Journal of Geophysical Research: Solid Earth*, 125(5), e2019JB017884. <https://doi.org/10.1029/2019JB017884>
- Ramos, V. A. (1999). Plate tectonic setting of the Andean Cordillera. *Episodes*, 22(3), 183–190. <https://doi.org/10.18814/epiugs/1999/v22i3/005>
- Ramos, V. A., Cristallini, E. O., & Pérez, D. J. (2002). The Pampean flat-slab of the Central Andes. *Journal of South American Earth Sciences*, 15(1), 59–78. [https://doi.org/10.1016/S0895-9811\(02\)00006-8](https://doi.org/10.1016/S0895-9811(02)00006-8)
- Ramos, V. A., & Folguera, A. (2009). Andean flat-slab subduction through time. *Geological Society, London, Special Publications*, 327(1), 31–54. <https://doi.org/10.1144/SP327.3>
- Ramos, V. A., & Kay, S. M. (1992). Southern Patagonian plateau basalts and deformation: Backarc testimony of ridge collisions. *Tectonophysics*, 205(1–3), 261–282. [https://doi.org/10.1016/0040-1951\(92\)90430-E](https://doi.org/10.1016/0040-1951(92)90430-E)
- Rawlinson, N., & Kennett, B. L. N. (2004). Rapid estimation of relative and absolute delay times across a network by adaptive stacking. *Geophysical Journal International*, 157(1), 332–340. <https://doi.org/10.1111/j.1365-246X.2004.02188.x>
- Rocha, M. P., Schimmel, M., & Assumpção, M. (2011). Upper-mantle seismic structure beneath SE and Central Brazil from P- and S-wave regional traveltimes tomography. *Geophysical Journal International*, 184(1), 268–286. <https://doi.org/10.1111/j.1365-246X.2010.04831.x>
- Rodríguez, E. E., Portner, D. E., Beck, S. L., Rocha, M. P., Bianchi, M. B., Assumpção, M., et al. (2020). Mantle dynamics of the Andean subduction zone from continent-scale teleseismic S-wave tomography. *Geophysical Journal International*, 224(3), 1553–1571. <https://doi.org/10.1093/gji/ggaa536>
- Russo, R. M., VanDecar, J. C., Comte, D., Mocanu, V. I., Gallego, A., & Murdie, R. E. (2010). Subduction of the Chile Ridge: Upper mantle structure and flow. *Geological Society of America Today*, 20(9), 4–10. <https://doi.org/10.1130/GSATG61A.1>
- Sanhueza, J., Yáñez, G., Buck, W. R., Araya Vargas, J., & Veloso, E. (2023). Ridge subduction: Unraveling the consequences linked to a slab window development beneath South America at the Chile triple junction. *Geochemistry, Geophysics, Geosystems*, 24(9), e2023GC010977. <https://doi.org/10.1029/2023GC010977>
- Schepers, G., van Hinsbergen, D. J. J., Spakman, W., Kosters, M. E., Boschman, L. M., & McQuarrie, N. (2017). South-American plate advance and forced Andean trench retreat as drivers for transient flat subduction episodes. *Nature Communications*, 8(1), 15249. <https://doi.org/10.1038/ncomms15249>
- Scire, A., Zandt, G., Beck, S., Long, M., & Wagner, L. (2017). The deforming Nazca slab in the mantle transition zone and lower mantle: Constraints from teleseismic tomography on the deeply subducted slab between 6°S and 32°S. *Geosphere*, 13(3), 665–680. <https://doi.org/10.1130/GES01436.1>
- Scire, A., Zandt, G., Beck, S., Long, M., Wagner, L., Minaya, E., & Tavera, H. (2016). Imaging the transition from flat to normal subduction: Variations in the structure of the Nazca slab and upper mantle under southern Peru and northwestern Bolivia. *Geophysical Journal International*, 204(1), 457–479. <https://doi.org/10.1093/gji/ggv452>
- Siebert, L., & Simkin, T. (2002). Volcanoes of the world: An illustrated catalog of Holocene volcanoes and their eruptions. *Smithsonian Institution, Global Volcanism Program, Digital Information Series*. GVP-3 <http://www.volcano.si.edu/world/>
- Simmons, N. A., Myers, S. C., Johannesson, G., & Matzel, E. (2012). LLNL-G3Dv3: Global P wave tomography model for improved regional and teleseismic travel time prediction. *Journal of Geophysical Research*, 117(B10), B10302. <https://doi.org/10.1029/2012JB009525>
- SIO. (1986). Scripps institution of oceanography, global seismograph network—IRIS/IDA [Dataset]. *International Federation of Digital Seismograph Networks*. <https://doi.org/10.7914/SN/II>
- Stern, C. R., & Kilian, R. (1996). Role of the subducted slab, mantle wedge and continental crust in the generation of adakites from the Andean Austral Volcanic Zone. *Contributions to Mineralogy and Petrology*, 123(3), 263–281. <https://doi.org/10.1007/s004100050155>
- Suárez, G., Molnar, P., & Burchfiel, B. C. (1983). Seismicity, fault plane solutions, depth of faulting, and active tectonics of the Andes of Peru, Ecuador, and southern Colombia. *Journal of Geophysical Research*, 88(B12), 10403–10428. <https://doi.org/10.1029/JB088iB12p10403>
- Thorkelson, D. J. (1996). Subduction of diverging plates and the principles of slab window formation. *Tectonophysics*, 255(1–2), 47–63. [https://doi.org/10.1016/0040-1951\(95\)00106-9](https://doi.org/10.1016/0040-1951(95)00106-9)
- Thorkelson, D. J., & Breitsprecher, K. (2005). Partial melting of slab window margins: Genesis of adakitic and non-adakitic magmas. *Lithos*, 79(1–2), 25–41. <https://doi.org/10.1016/j.lithos.2004.04.049>
- Thorkelson, D. J., & Taylor, R. P. (1989). Cordilleran slab windows. *Geology*, 17(9), 833–836. [https://doi.org/10.1130/0091-7613\(1989\)017<0833:CSW>2.3.CO;2](https://doi.org/10.1130/0091-7613(1989)017<0833:CSW>2.3.CO;2)
- Universidad de Chile. (2012). Red Sismológica Nacional [Dataset]. *International Federation of Digital Seismograph Networks*. <https://doi.org/10.7914/SN/C1>
- Veloso, E. A. E., Anma, R., & Yamazaki, T. (2005). Tectonic rotations during the Chile Ridge collision and obduction of the Taitao ophiolite (southern Chile). *Island Arc*, 14(4), 599–615. <https://doi.org/10.1111/j.1440-1738.2005.00487.x>
- Wessel, P., Luis, J. F., Uieda, L., Scharroo, R., Wobbe, F., Smith, W. H. F., & Tian, D. (2019). The Generic Mapping Tools version 6. *Geochemistry, Geophysics, Geosystems*, 20(11), 5556–5564. <https://doi.org/10.1029/2019GC008515>
- Wiens, D. A., & Magnani, M. B. (2018). Solid Earth response of the Patagonia Andes to post-little ice age glacial retreat [Dataset]. *International Federation of Digital Seismograph Networks*. [https://doi.org/10.7914/SN/IP\\_2018](https://doi.org/10.7914/SN/IP_2018)
- Wiens, D. A., Nyblade, A., & Aster, R. (2007). IPY POLENET-Antarctica: Investigating links between geodynamics and ice sheets [Dataset]. *International Federation of Digital Seismograph Networks*. [https://doi.org/10.7914/SN/YT\\_2007](https://doi.org/10.7914/SN/YT_2007)